universität wien

DIPLOMARBEIT / DIPLOMA THESIS

Titel der Diplomarbeit / Title of the Diploma Thesis

„ Time-Domain Biomolecular Interference “

verfasst von / submitted by

Georg Erich Richter, BSc

angestrebter akademischer Grad / in partial fulfilment of the requirements for the degree of

Magister der Naturwissenschaften (Mag.rer.nat.)

Wien, 2018

Studienkennzahl lt. Studienblatt:	A 190 406 412
Studienrichtung lt. Studienblatt:	Lehramtsstudium UF Mathematik UF Physik
Betreut von:	Univ. Prof. Dr. Markus Arndt

Abstract

Quantum phenomena have gained public interest due to their contradiction to our classical intuition. In quantum physics the delocalization and propagation of objects through space can be described by matter-waves. This holds for sub-microscopic particles but apparently fails for more massive objects as observed in our daily life. Matter-wave interferometry has been established for novel tests of the linearity of quantum mechanics as well as a reliable tool for analysis of the internal properties of molecules.
Measurements with biomolecules using the Optical TIme-domain MAtter-Wave interferometer (OTIMA) are now exploring quantum physics at the interface to biomolecular science. This thesis presents first interference measurements with a complex polypeptide: the antibiotic Gramicidin with a mass of 1882 amu consisting of 15 amino acids.
This demonstration requires the preparation of isolated particles in the gas phase in a stable molecular beam, which is realized by laser desorption of the molecules into a supersonic beam of argon atoms. The desorption efficiency shows strong dependence on the laser pulse length, wavelength and energy, being optimal for UV desorption and picosecond pulse lengths. This source technique enabled the first realization of a neutral beam of artificial proteins with masses exceeding 20 000 amu.
The successful source experiments enabled peptide quantum interference with inclusion of more realistic beam properties to the contrast. This thesis presents the mathematical formalism describing the beam propagation through the interferometer, which allows a reliable prediction of the experimental results. The simulations are in good agreement with the real data.

Zusammenfassung

Quantenmechanische Erscheinungen sorgen gerne für öffentliches Interesse, da sie sich nicht mit unseren Erwartungen aus dem Alltag erklären lassen. Zwar kann mit dem Superpositionsprinzip die Delokalisierung und Fortbewegung von Objekten durch den Raum in Form von Materie-Wellen beschrieben werden, jedoch scheint diese Beschreibung nur für submikroskopische Teilchen gut zu funktionieren, während sie an massereicheren Objekten des Alltags scheitert. Materie-Wellen-Interferometer zeigen sich als zuverlässiges Werkzeug, um die Linearität der Quantenmechanik zu testen. Gleichzeitig ermöglichen sie die Analyse interner Eigenschaften von Molekülen.
Messungen an Biomolekülen am Optical TIme-domain MAtter-wave Interferometer (OTIMA) bilden somit eine Schnittstelle zwischen der Quantenmechanik und der Biophysik. Diese Arbeit zeigt die ersten Interferenzmessungen mit einem komplexen Polypeptid: das Antibiotikum Gramicidin. Es besteht aus 15 Aminosäuren und hat eine Masse von 1882 amu.
Für den Nachweis von quantenmechanischen Phänomenen an einem solchen Molekül wird die Aufbereitung von isolierten Teilchen in der Gasphase in Form eines Molekülstrahles benötigt. Dies geschieht mittels Laserdesorption in eine Überschallexpansion von Argon-Atomen. Es zeigt sich eine starke Abhängigkeit der Desorptionseffizienz von der Laserpulslänge, der Wellenlänge und der Energie, optimal für Pikosekunden-Pulslängen und UV-Wellenlängen. Diese Quellmethode ermöglichte es erstmals einen neutralen Molekülstrahl von Proteinen mit Massen über 20 000 *amu* zu formen.
Die erfolgreichen Quellexperimente erlaubten es die Auswirkungen von realistischeren Strahleigenschaften in den Peptid- Interferenzmessungen zu berücksichtigen. Dafür wird der mathematische Formalismus, welcher die Fortbewegung des Molekülstrahles durch das Interferometer beschreibt, erläutert. Dieser ermöglicht eine zuverlässige Vorhersage der experimentellen Daten, deren Übereinstimmung mit den gemessenen Daten gezeigt wird.

Contents

1 Introduction

Within the last centuries science revealed many new hypothesis and theories to better describe the world we live in. Over the years some of them lost their validity [1] or even the public attention [2], but some persisted and gained high reputation in the community. One well known example of such a theory is quantum mechanics.
From Planck's description of thermal radiation in 1900 [3], over Einstein's discovery of the photoelectric effect in 1905 [4] to the quantization as Eigenwertproblem by Schrödinger in 1926 [5], quantum theory has been firmly established in physics and has passed all experimental tests ever since. Nowadays it is a well accepted theory with wide ranging applications beyond the microscopic world.
The contradiction to our classical intuition creates significant and interdisciplinary interests in quantum theory. One good example is the wave-particle-duality, raised out of the incompatibility of Young's claim on the wave-character of light [6] and Einstein's description as a particle [4]. In 1923 Louis de Broglie proposed the same dualism for particles [7] and attributed to them a wavelength of

$$\lambda_{\mathrm{dB}} = \frac{h}{mv}. \tag{1}$$

Here h denotes the Planck constant, m the mass and v the velocity of the particle. Diffraction of electrons [8] and neutrons at crystal surfaces [9], followed by interferometry of atoms [10, 11], dimers [12, 13] and nowadays of more massive molecules [14] revealed the wave-character of particles of high temperature and complexity. This leads to the question if it could be possible to observe such quantum phenomena in our daily life. Everyone who once had to choose between two lines at a supermarket checkstand may imagine how favorable it would be to find oneself in a superposition of the left and right line to end up in the faster one. For sure this can be denied due to the unfeasible short wavelength of macroscopic objects, which is around $\lambda_{\mathrm{dB}} \approx 10^{-36}$ m for a person with a mass of 70 kg moving with a speed of 1 m/s [15]. Even if it were possible to detect wavelengths at this length scale the superposition of macroscopic states is further suppressed by phase averaging [15] and decoherence phenomena [16]. The coupling of a quantum object to its environment causes complex entanglement and reduces the visibility of quantum phenomena of the individual system [17]. Some theories highlight the interplay between gravity and quantum mechanics as a role in this process [18, 19]. Others predict that decoherence is caused by interaction with undetectable dark matter [20]. However, models try to include such stepwise transitions from quantum to classical mechanics considering a continuous collapse of the wave function. Therefore Continuous Spontaneous Localization models (CSL) include mass dependent interactions with a stochastic background field, whereas a model of Penrose and Diósis

[21, 22] considers interaction with gravity. Even though there have been proposals on how to test the model from Penrose and Diósis [23] there's no experimental data yet. For CSL several experiments led to a limitation of the parameter space, but still non of the actual experiments are capable of testing collapse mechanisms or gravitational interaction with macroscopic superposition states in the mass range of $10^9 - 10^{10}$ amu.
Interferometry is very sensitive to a colapse of the wavefunction too [24] and therefore allows testing the mass limits of quantum mechanics, independent of the underlying model. The current upper bound with a mass of $m = 10\,123$ amu is set by the group of Markus Arndt at the University of Vienna [25]. Their interferometers take advantage of the superposition principle to delocate and recombine molecules during their travel through grating arrangements. This imprints a periodic modulation of the molecular beam intensities, which can be red with nanometer accuracy, but can easily be shifted in the presence of external forces acting on the molecules. This allows extracting electronic, magnetic, optical and structural properties of molecules beside of testing the superposition principle [26]. Hence, matter-wave interferometry has the potential to establish as a high precision metrology tool for molecules in an isolated environment. Using biomolecules, the building blocks of life consisting of several amino acids, opens research fields at the interface between quantum physics, physical chemistry and even (clinical) medicine.

2 Theory

The interference measurements with biomolecules discussed in this thesis rely on the preparation of isolated molecules in the gas phase followed by diffraction and recombination in a Talbot-Lau-Interferometer (TLI). For most of the biological molecules simple heating is not sufficient to force intact transition to the gas phase. Vibrations on the picosecond time scale [27] as well as unfolding on the nano- up to microsecond time scale lead to degeneration of the biomolecules at high temperatures [28]. A cooling mechanism is required to keep molecules intact after evaporation.
Therefore this section focuses on supersonic gas expansion as one possible cooling mechanism. It is followed by a description of the interference setup itself, a mathematical description of the interference process and options to distinguish between quantum phenomena and classical shadow effects within the interference measurements.

2.1 Supersonic Gas Expansion

Supersonic nobel gas expansion leads to directed, fast and cold molecular beams. Injection of analyte molecules into the atomic expansion delivers a well defined and directed mass motion with additional cooling of the particles [29]. The experimental setup currently in use takes advantage of this behavior by injecting molecules with laser-desorption, demonstrated for masses up to 20 kDa. It is described in Chapter 3.1 in more detail.
In a simple picture the gas expansion from high to low pressure through a nozzle leads to a supersonic beam as long as the nozzle diameter D exceeds the mean free path of the gas $D \gg \lambda_{\mathrm{m}}$. Due to many collisions the atoms and the injected molecules transform a lion share of their translational motion and internal energy into a directed molecular flow. This is described by gas dynamic equations [30]. The mean free path is $\lambda_{\mathrm{m}} = \frac{1}{n_0 \sigma}$ [31], where n_0 denotes the particle density inside the high pressure reservoir and σ the collision cross section of the particles[1]. In case $D \ll \lambda_{\mathrm{m}}$ the expansion is called effusive and results in a velocity distribution that can be well approximated by a Maxwell-Boltzmann distribution.
For high backing pressure p_0 one can neglect the heat transfer and viscosity of the gas and describe the expansion as an adiabatic process [32], which conserves the sum of kinetic energy and enthalpy

$$\frac{1}{2}mv(x_0)^2 + H(x_0) = \frac{1}{2}mv(x)^2 + H(x) = const, \tag{2}$$

where m is the particle mass and $v(x)$ is the average flow velocity at position x. The molar enthalpy $H = U + pV$ is given in terms of the internal energy

[1] For random walking particles in the gas phase with a Maxwell-Boltzmann velocity distribution one can use $\lambda_m = \frac{1}{\sqrt{2}\pi n_0 d^2}$, where d denotes the diameter of the particles.

U and the flow work pV which is caused by the pressure gradient [30] and described in terms of the pressure p and the volume V. For maximum average flow velocity the entire enthalpy is converted to kinetic energy ($H(x) \approx 0$), via collisions between neighboring molecules. Due to the random walk of particles inside the limited high pressure reservoir the average velocity $v(x_0)$ at the nozzle location x_0 is assumed to vanish. Assuming an ideal gas, with a temperature T and a molar heat capacity[2] C_p, $H(T) = C_\mathrm{p}T$ holds and leads to a maximum velocity of the molecular beam:

$$v_{max} = \sqrt{\frac{2C_\mathrm{p}T_0}{m}}, \tag{3}$$

where T_0 is the temperature of the gas inside the high pressure reservoir. Compression and rarefaction of gas by sound waves cause heat transfer due to thermal gradients. In many cases these gradients are small enough to neglect a transport of heat and the propagation of sound can be treated as an adiabatic process [33]. Therefore the velocity of sound v_s is described in terms of the adiabatic coefficient $\gamma = C_\mathrm{p}/C_\mathrm{v}$, the molecule mass m and the Boltzmann constant k_B:

$$v_\mathrm{s}(T) = \sqrt{\frac{\gamma\ k_\mathrm{B}T}{m}}. \tag{4}$$

Decreasing the temperature lowers the speed of sound. An expansion is supersonic if the average velocity $v(x)$ is bigger than the speed of sound $v_\mathrm{s}(T(x))$. In terms of the Mach number, $M(x) = v(x)/v_\mathrm{s}(x) > 1$. According to (3) and (4) this is fulfilled at some point during the cooling of the gas. Noble gases like helium, neon or argon with an initial temperature $T_0 = 300$ K reach maximum velocities in the range of $500 - 1000$ m/s and Mach numbers above 20 [34]. Formula (5) and (6) use the ideal gas law to calculate the temperature T and the gas density ρ with respect to the Mach number during the expansion. For large nozzle distances x and atoms the asymptotic approximations for T and ρ on the right hand side of the formula hold. Here B, F and x_0/D are constants depending on the adiabatic coefficient γ [35]:

$$\frac{T}{T_0} = \left(\frac{p}{p_0}\right)^{\frac{\gamma-1}{\gamma}} = \left(1 + \frac{\gamma-1}{2}M(x)^2\right)^{-1} \overset{x\gg D}{\rightarrow} \frac{T(x)}{T_0} = B\left(\frac{D}{x-x_0}\right)^{2(\gamma-1)}, \tag{5}$$

$$\frac{\rho}{\rho_0} = \left(\frac{p}{p_0}\right)^{\frac{1}{\gamma}} = \left(1 + \frac{\gamma-1}{2}M(x)^2\right)^{-\frac{1}{\gamma-1}} \overset{x\gg D}{\rightarrow} \frac{\rho(x)}{\rho_0} = F\left(\frac{D}{x-x_0}\right)^{2}. \tag{6}$$

Close to the nozzle, the pressure ratio has a major influence on the cooling and molecular velocity spread. Further downstream they are both dominated by the ratio of nozzle diameter to the distance. At a certain distance

[2] C_p denotes the heat capacity for constant pressure, whereas C_v denotes a constant volume.

the approximation of an idealized continuum model is no longer valid and the molecules are isolated in a collision-free environment. The decrease of the collision-rate also limits the energy transfer in the beam. This marks the point where cooling stops [34].
For the three temperatures associated with the molecular degrees of freedom (translational, rotational and vibrational) this happens on different timescales. Cooling of the vibrational modes, typically separated by $0.01 - 0.1$ eV requires higher collision rates than cooling of the rotational modes with energy gaps in the range of $0.001 - 0.01$ eV [36] or even translations with a continuous energy spectrum. Vibrational cooling therefore occurs dominantly inside the nozzle [37, 38] and vibrational modes freeze out[3] first, followed by the rotational degrees of freedom [39]. Translational cooling further remains and decouples the internal from the translational modes [40]. This leads to the general assumption $T_{\mathrm{vib}} > T_{\mathrm{rot}} > T_{\mathrm{trans}}$.
Kinetic models reveal a point where the velocity components along the expansion axis remain constant, while perpendicular components still seem to narrow. This is caused by purely geometrically effects, because molecules with large perpendicular velocity components are driven off by their own momentum [41]. This allows to define two different translational temperatures: the parallel temperature $T_{\parallel}$ and the perpendicular temperature $T_{\perp}$ [32]. The end of cooling for the parallel, translational temperature $T_{\parallel}$ is associated with a terminal Mach number M_{T}. For monodisperse gases this number is calculated by [34]:

$$M_{\mathrm{T}} = G \cdot \left(\sqrt{2}\sigma\rho_0 D\epsilon\right)^{\frac{\gamma-1}{\gamma}}, \tag{7}$$

where $G = ((\gamma+1)/2)^{\gamma/(\gamma-1)}$ (smaller than 2.1 for all gases), the collision cross section σ, the gas density ρ_0 in the high pressure reservoir and ϵ, a collisional effectiveness parameter denoting the maximal percental change of the mean velocity per collision ($0.2 - 0.3$ for Argon at 50 Torr [34]). For stronger cooling $\rho_0 D$ needs to be increased. For a fixed initial temperature one can exchange the gas density ρ_0 with the initial pressure p_0 in the first reservoir leading to $\rho_0 D \to p_0 D$.
The assumption of an idealized continuum fails when the background density becomes comparable to that of the expanding gas. The beam then travels through a shock zone, where collisions with the background gas randomize the velocity distribution and stop the supersonic expansion. Two kinds of shock zones restrict the expansion area. A parabolic one along the propagation axis and a nearly flat one orthogonal to the beam axis - the Mach disk [42]. The thickness of the shock zone depends on the absolute value of the background pressure p_{B}, while the position of the Mach disk is determined

[3] To freeze out denotes the situation where degrees of freedom stop the exchange of heat and fall out of the thermal equilibrium.

by the ratio of initial and background pressure. In a simple approximation the Mach disk location x_{M} is calculated with [35]:

$$x_{\mathrm{M}} = 0.67D\sqrt{\frac{p_0}{p_{\mathrm{B}}}}. \tag{8}$$

A cold molecular beam can be obtained by seeding small amounts of the molecules into the atomic beam expansion. Collisions with the lighter carrier gas accelerate the molecules to a well defined kinetic energy [34], limited by the terminal flow velocity of the lighter carrier gas. In many applications molecules are vaporized in the high pressure reservoir in order to be co-expanded through the nozzle with the carrier gas. The heavier molecules are even better centered on the jet axis than the carrier gas due to lower collision efficiency orthogonal to the beam axis [30]. However, for perpendicularly inserted molecules desorbed from a nearby surface, collisions with the carrier gas have proven to be sufficient to damp orthogonal velocity components, to create a directed mass flow along the expansion axis [43] and to further provide molecular cooling of the internal degrees of freedom [44]. The efficiency of such cooling is limited by the mass ratio of carrier gas and seeded molecules. For insufficient energy transport the heavier molecules lag behind the carrier gas. This behavior is called velocity slip [45] and usually molecules sustained such a slip reveal a higher internal energy than molecules without a slip [44]. In a certain amount this can be compensated by increasing the collision rate due to earlier injection of the molecules into the atomic beam expansion or increasing the initial pressure p_0.

The velocity distribution of the molecular beam at any position x behind the nozzle is described by:

$$P_{\mathrm{sonic}}\left(v'\right) \propto {v'}^3 \exp\left[-\frac{m\left(v'-v(x)\right)^2}{2k_{\mathrm{B}}T(x)}\right]. \tag{9}$$

Assuming full acceleration of the molecules their velocity can be approximated by the maximum of the carrier gas $v(x) = \sqrt{2[H(T_0) - H(T(x))]/m}$ (see Equation (2)). The temperature $T(x)$ in dependence of the nozzle distance x can either be calculated using Equation (5), or, in case of missing knowledge of the constants, using a monoatomic approximation [35]:

$$T(x) = T_0\left[1+\frac{1}{3}\left(3.26\left(\frac{x}{D}-0.075\right)^{2/3} - \frac{2}{3.26\left(\frac{x}{D}-0.075\right)^{2/3}}\right)^2\right]^{-1}. \tag{10}$$

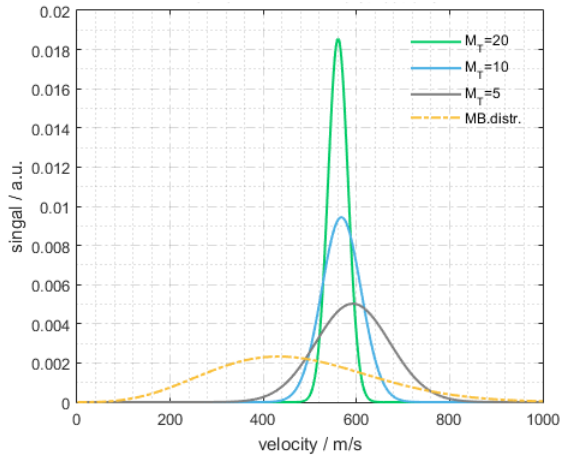

Figure 1: The velocity distributions for argon molecules with $m = 40$ amu expanding from a reservoir of $T_0 = 300$ K. The orange line corresponds to the Maxwell-Boltzmann distribution of effusive beams. The supersonic beam distribution is shown for different terminal Mach numbers ($M_\mathrm{T} = 5, 10, 20$). For each distribution the area under the curve is normalized.

For simulations of the final velocity distribution of the supersonic beam in Figure 1 the maximum flow velocity $v(x) = v_\mathrm{max}$ from Equation (3) and the final parallel translational temperature $T_\parallel$ are used to account for the final state of the molecular beam.
The temperature is calculated using Equation (5) and different terminal Mach numbers. Figure 1 also shows the Maxwell-Boltzmann velocity distribution[4] of an effusive beam. In all simulations, argon is used with a mass of $m = 40$ amu and an initial temperature of $T_0 = 300$ K. The velocity distributions are normalized. Compared to the distribution of the Maxwell-Boltzmann beam (orange line) the supersonic beam (grey $M_\mathrm{T} = 5$, blue $M_\mathrm{T} = 10$, green $M_\mathrm{T} = 20$) reveals higher average velocities with smaller deviations due to cooling. This even holds for low Mach numbers like $M_\mathrm{T} = 5$, where the distribution is about two times narrower than the Maxwell-Boltzmann velocity distribution. For increasing Mach numbers the average velocity decreases.
Subsequently the cooled and isolated molecules are guided through a Talbot-Lau-Interferometer. This prepares coherent matter-waves to show the quantum phenomena of the molecules.

[4]The simulation of the Maxwell-Boltzmann distribution uses the velocity density $P(v) \propto v^3 \exp(-mv^2/(2k_\mathrm{B}T))$.

2.2 The Talbot-Lau-Interferometer

Interferometry with matter-waves has proven to be a reliable tool to show quantum phenomena even for particles of high mass. This section focuses on the theory of matter-waves and their usage in Talbot-Lau-Interferometers to reveal the wave-particle duality.
In the absence of time-dependent fields the Helmholtz equation is equivalent to the stationary Schrödinger equation. Therefore the behavior of a matter-wave is in close analogy to the propagation of light [46]. Assume a monochromatic, coherent, electro-magnetic plane wave $E(\vec{x}) = A(\vec{x}) \times \exp(k_0 \cdot z)$, with a wave amplitude A and a wave number k_0. The wave propagates along the z-axis and hits an object with an opening transmission function $S(x, y)$ and a diameter ρ. Interaction with the obstacle modifies the wave amplitude $A(\vec{x})$. The intensity of modulation is dominated by the diameter of the aperture ρ, the wavelength $\lambda_0 = 2\pi/k_0$ and shrinks with the aperture distance L. The Fresnel number F marks the effective interaction area of the obstacle and the wave:

$$F = \frac{\rho^2}{\lambda L}. \tag{11}$$

For $F \gg 1$, which is equal to a large diameter or a short wavelength, the amplitude $A(\vec{x})$ stays almost constant, while $F \ll 1$ indicates a position dependent modulation of the amplitude [47]. This modulation leads to the well known diffraction patterns. Using Huygens principal and summing up the expansion of spherical waves from each point of the opening allows the calculation of the wave amplitude's modulation. The resulting integrals cannot be solved analytically [48]. However, Taylor expansion of the exponent and neglecting higher order terms lead to the Kirchhoff-Fresnel-Integral[5]

$$E(\vec{x}) = \frac{i}{\lambda_0 z} \iint_{S(x_0,y_0)} dx_0 dy_0 \; E(x_0, y_0) \exp\left(-\frac{i k_0}{2 z}\left[(x_0 - x)^2 + (y_0 - y)^2\right]\right). \tag{12}$$

For distances $L > \rho^2/\lambda_0$ one can neglect the quadratic terms in the exponent. This leads to the Fraunhofer integral, which describes the wave behavior in the far-field regime. Here the curvature of the wave front can be disregarded and the propagating wave is approximated by a planar wave. The regime of shorter distances, where $L < \rho^2/\lambda_0$, is called the near-field, where the curvature of the wave front needs to be taken in account.
This thesis focuses on interferometers working in the near-field regime. Compared to far-field interferometers, like the Mach-Zehnder [49] or the Ramsey-Bordé [50] setup, which rely on path separation of the beam, near-field inter-

[5] Still, the Kirchhoff-Fresnel-Integral is solvable only for a very limited number of special arrangements.

ferometers do not require transversal coherence of the initial molecular beam [51]. In many setups the transverse coherence parallel to the grating vector is gained by collimation of the beam. Therefore the relaxed collimation requirement of near-field-Interferometers allows using a higher molecular flux. A near-field interferometer is based on the Talbot effect [52]. When monochromatic light from a point source illuminates a periodic structure, such as a grating, self images of the structure appear at multiples of a certain distance. The minimal distance is called the Talbot length L_{T}. It is determined by the grating period d and the wavelength λ:

$$L_{\mathrm{T}} = \frac{d^2}{\lambda}. \tag{13}$$

For odd multiples of the Talbot length the pattern is shifted by half the grating period. For even integers the pattern is an exact self-image[6]. In practice the molecule-grating interaction modulates the phase which lets the self-imaging effect appear at distances slightly smaller than the Talbot length [53]. At fractional distances self-images with smaller spatial periodicity appear. The periodic structures at different lengths sum up to a periodic $2D$ pattern, the Talbot carpet [54].
Such a one-grating interferometer requires spatial and temporal coherence of the incident wave. This requirement is overcome by placing a second identical grating $G^{(2)}$ parallel to the first one in the Talbot distance, as first discovered by Lau [55]. Each opening of the first grating $G^{(1)}$ then acts as a point source as described by the Van Cittert-Zernike theorem of optics [56, 57]. The propagating wavelets reach sufficient transverse coherence to cover at least two slits of $G^{(2)}$ with a spatially well-defined phase relation. Diffraction in a distance of L_{T} behind the grating leads to an intensity modulation with periodicity d - an interferometric self-image of the grating.
From here on a symmetric configuration of a Talbot-Lau-Interferometer (TLI) is assumed, where all the gratings have the same periodicity and same inter-grating separation. Observation of interference is also possible with an asymmetric grating arrangement as shown in [58]. The combination of two gratings allows detection of fringe patterns for spatially incoherent waves too [59]. According to de Broglie, particles can also be described by waves of wavelengths λ_{dB}. The treatment above holds for matter-waves. Small grating openings of $G^{(1)}$ deliver sufficient transverse coherence in momentum. This can be explained with Heisenberg's position momentum uncertainty [60], where the spread in momentum is a consequence of the narrow collimation of the spatial position of the particles at $G^{(1)}$.
The interference pattern can be visualized by detectors of high spatial resolution [61] or by using a third identical grating $G^{(3)}$ positioned at a Talbot length behind $G^{(2)}$. The grating acts as a mask for the interference pattern.

[6] Other literature therefore define the Talbot length as $L_{\mathrm{T}} = \frac{2d^2}{\lambda}$.

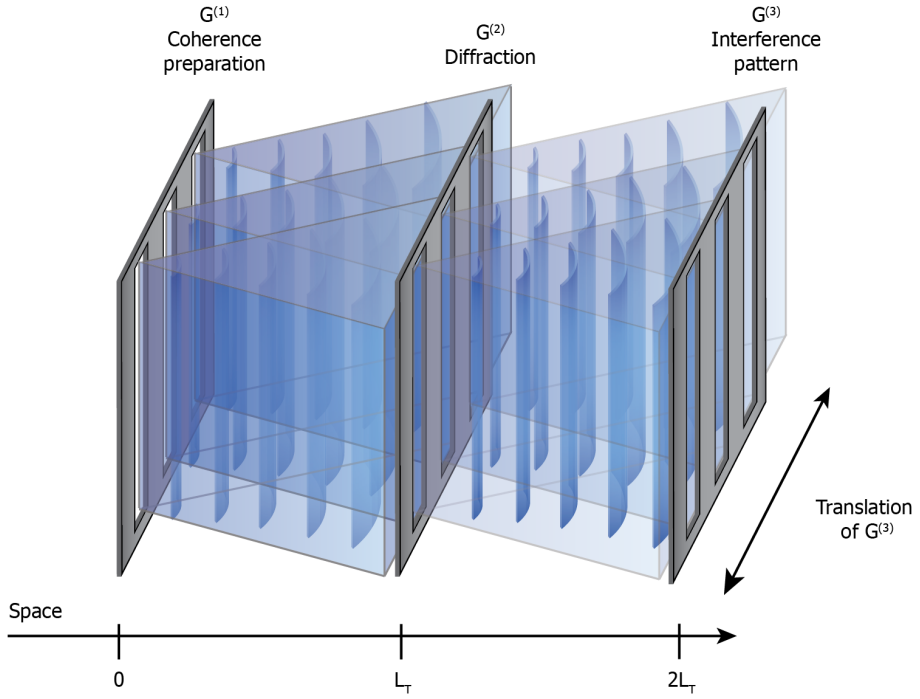

Figure 2: A schematic of a Talbot-Lau-Interferometer (TLI), where all gratings have the same period. The first and second grating ($G^{(1)}$ and $G^{(2)}$) modulate the molecular beam and create self images at multiple distances of the Talbot length L_{T}. Those patterns are sampled by the third grating $G^{(3)}$. Translation of the last grating leads to a modulation of the molecular flux with a period d.

Translation along the grating vector modulates the particle flux behind the third grating with the periodicity d. The scheme of such a TLI is shown in Figure 2.
In many TLI setups the particle count rate in dependence of the grating shift is assumed to result in a sinusoidal modulation of the signal S. It is common to use the visibility $\mathcal{V}$ as a measure for the fringe contrast [62]:

$$\mathcal{V} = \frac{S_{\mathrm{max}} - S_{\mathrm{min}}}{S_{\mathrm{max}} + S_{\mathrm{min}}}. \tag{14}$$

However, if the fringe pattern differs from a sinusoidal modulation it is favorable to define the normalized signal contrast S_{N} instead. This is discussed in Chapter 2.4.3.
For Talbot-Lau-Interferometers of fixed length the required grating period scales with $d \propto \sqrt{\lambda_{\mathrm{dB}}} \propto 1/\sqrt{m}$. This is a huge advantage compared to

the linear scaling of far-field experiments, since it is not possible to produce gratings with arbitrarily small grating periods.
Interference measurements at a fixed grating period d and interferometer length require slowing of massive particles to match Equation (13), where $\lambda \to \lambda_{\mathrm{dB}} = h/(mv)$. This extends the interaction time of the molecules with the grating walls. Via van der Waals and Casimir-Polder forces [63, 64], depending on the distance of the particles and the gratings, additional phases are imprinted onto the molecular beam. This leads to a position dependent diffraction spread behind the second grating and smears out the near-field interference pattern.
The Optical TIme-domain MAtter-wave interfereometer (OTIMA) circumvent such disadvantages by only using optical gratings realized by three retro-reflected laser beams [65].

2.3 OTIMA: Interference in the Time-Domain

An all optical Talbot-Lau-Interferometer requires absorptive optical gratings and efficient depletion channels to prepare spatial coherence with the first grating and mask the interference pattern with the third grating. Even though the realization with pure phase gratings had been done before [66, 67], it requires transverse coherence of the incident beam which is hard to fulfill. Absorptive optical gratings were realized for atoms [68] by resonant excitation to dark states. This makes the atoms invisible for light. Such a resonant excitation schemes cannot be readily generalized to a wide range of particles. In case of molecules the excitation is followed by excited state dynamics. The absorbed energy gets redistributed over the internal degrees of freedom. This increases the internal energy but probably will not lead to a detectable change of the molecular state, appearance or behavior[7]. Therefore resonant excitation schemes are hardly possible for molecules.
A universal absorptive beam splitter is established in OTIMA by retro-reflecting the Vacuum Ultra-Violet (VUV)-light of lasers as shown in Figure 3. For a wide range of organic molecules, organic and atomic clusters and Tryptophan-based polypeptides the VUV-photon-energy exceeds the ionization energy. Absorption of a photon is followed by ionization of the molecules and allows depletion of the beam. Also fragmentation of molecules or weakly bound clusters after absorption is a possible depletion mechanism. In case of cluster beams the recoil of the dissociation-process has to be sufficient to remove the fragments from the beam [69]. Otherwise they would distort the mass spectra of smaller cluster. However, this is no problem for molecules with clearly distinguishable fragment masses.

[7] Still detection might be possible by inducing photoisomerization and detection of only fluorescent conformations.

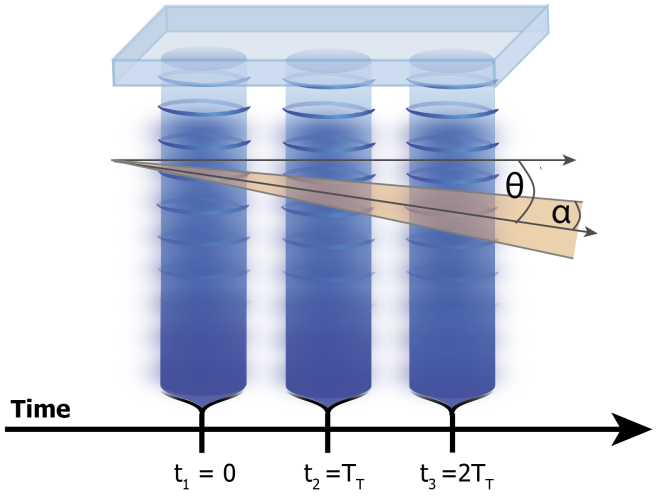

Figure 3: OTIMA uses retro-reflection of three laser beams on a single mirror surface to realize standing waves. Absorption of VUV-photons in the antinodes of the standing waves removes particles from the beam either by ionization or fragmentation. Particles in the nodes stay intact. Therfore the retro-reflected waves act like pure material gratings. Pulsed beam sequences with a delay around the Talbot time T_T form a TLI in the time-domain. Here θ denotes a tilt of the molecular beam along the grating vector, whereas α denotes the divergence of the beam.

In the OTIMA setup each of the three optical gratings acts as an absorptive mask. Particles traversing the antinodes are removed, while the others remain. This results in a modulation of the molecular beam with a period of $\lambda_\mathrm{L}/2$. Here λ_L corresponds to the laser wavelength. The opening fraction of each grating can be reduced by increasing the laser power, since the probability of absorbing photons even in the close vicinity of the nodes increases. The phase modulating character of the first and third optical grating is unimportant. The additional phase from interaction with the light field of the first grating can be neglected due to the random phase distribution of the molecular beam. A phase shift of the third grating has no influence on the detected flux. Only the second grating operates as absorptive and phase grating, depleting the beam and imprinting a phase-shift onto the remaining particles.
In addition to the spatial separation of the optical gratings, OTIMA operates in the time-domain by using pulsed VUV-lasers. This eliminates all velocity-dependent phase shifts [54, 70], but not the Coriolis force which could be compensated by vertical alignment of the interferometer [71]. Two particles with the same mass m, but different velocities $v_1 < v_2$ have differ-

ent Talbot lengths $L_k = mv_k d^2/h$, $k \in \{1, 2\}$ where $L_1 < L_2$. Therefore a fixed grating position in space only fits to a certain velocity class of particles. Missing velocity selection smears out the interference pattern and decreases the contrast. To circumvent this issue, one can fix the timing of the gratings instead. With $T = L/v$ this leads to the so called Talbot time T_T:

$$T_T = \frac{md^2}{h}. \tag{15}$$

It is determined by the grating period d, the particle mass m and the Planck constant h, but it is independent of the molecular velocity. This allows an extension of the optical grating along the propagation direction of the molecular beam to guarantee interaction independent of the molecular position and the velocity. For each particle the pulsed optical grating appears for a limited time at the right position to match the Talbot condition. Still, single interaction of the particles with each grating before detection requires a trade-off between the particle velocity, the interaction time and the beam waist in the flight direction. The interaction time needs to be limited to short pulses, to guarantee traversing molecules can be assumed to rest during the pulse. To circumvent detection of particles which skipped grating interaction, the source needs to be pulsed too. The same holds for the detection unit, which selects only those particles which had interacted with all three gratings.

2.4 Mathematical Description of the OTIMA Model

The mathematical description of a molecular beam propagating through a TLI has been presented previously [24, 72, 73]. An adaption to the OTIMA setup with all-optical gratings is presented in [53, 74–77]. Based on the previous development, the OTIMA formalism is reviewed and modified to account for slightly tilted beams with respect to the grating vector.
In the following section, the spatial extension of the particles is treated to be small enough to neglect Rayleigh and Mie scattering, which is fulfilled for particles much smaller than the grating period [53]. Absorption of a single photon is assumed to be enough to remove a particle from the beam. The gratings show modulation with a period d only in the x-direction and are invariant to translations in the y-z-plane. The spatial expansion of the molecular beam along the z-axis, short enough grating pulses to neglect a change of the particle positions and a homogeneous laser beam profile along the z-axis require a restriction of the molecular beam tilt θ. The travel-distance along the x-axis of a molecule during interaction with the laser for a time τ has to be small compared to the grating period $v_x\tau \ll d = \lambda_L/2$.

For the following calculations the tilt is restricted[8] to $\theta \leq 100$ mrad $\approx v_x/v_z$. This allows the usage of the paraxial approximation. Furthermore, applying the eikonal approximation enables separation of the longitudinal and the transversal parts of the beam state. This reduces the calculations to a one-dimensional modulation of the beam along the x-axis, where the initial beam state is represented by the density matrix $\rho(x, x')$.

2.4.1 Free Propagation and Transmission through Gratings

One method to describe the molecular beam in terms of phase space variables is to use the one-dimensional Wigner function $w(x, p)$, where x denotes the position and p the momentum of the states. The Wigner function is defined by the following transformation of the position density matrix $\rho(x, x') = \langle x| \hat{\rho} |x'\rangle$ [78]:

$$w(x,p) = \frac{1}{2\pi\hbar} \int ds\, e^{ips/\hbar} \langle x - \frac{s}{2}| \hat{\rho} |x + \frac{s}{2}\rangle . \tag{16}$$

In this framework the propagation of the molecular beam for a time t is represented by an asymptotic expansion of the free Green function. The Green function is the solution of the Hamiltonian $\mathcal{H}_0 = p^2/(2m)$ in absence of external fields [79]. The Wigner function therefore transforms to

$$w(x,p) \to w\left(x - \frac{p\,t}{m}, p\right). \tag{17}$$

The framework of Wigner functions allows simple comparison with expectations of classical phase space dynamics based on ballistic trajectories. Under free evolution the classical phase space density $f(x, p)$ transforms like the Wigner function [72]:

$$f(x,p) \to f\left(x - \frac{p\,t}{m}, p\right). \tag{18}$$

For a more general case, a position shift due to a constant acceleration a parallel to the x-axis is included. This allows to take gravitational, electric or magnetic forces into account. To include a tilt of the molecular beam an additional shift due to the constant momentum $p_\theta = mv\tan(\theta)$ parallel to the x-axis is added. The tilt momentum p_θ has to be distinguished from the general momentum distribution p of the molecular beam. Transformation of the Wigner function after free propagation for a time t therefore changes to

[8] This value is based on the assumptions of a molecular beam with a longitudinal velocity $v_z = 100$ m/s and a grating interaction time of $\tau \leq 10$ ns. This restricts the transverse velocity to $v_x \leq 10$ m/s [53].

$$w\left(x,p\right) \rightarrow w\left(x-\frac{p\,t}{m}+\frac{p_\theta t}{m}+\frac{a\,t^2}{2},p-p_\theta-a\,m\,t\right), \tag{19}$$

which also holds for classical descriptions.
Transmission through a grating $G^{(\mathrm{k})}$ is described by a complex transmission function $t^{(\mathrm{k})}(x)$, which acts on the position density matrix:

$$\rho(x,x') \;\rightarrow\; t^{(\mathrm{k})}(x)\rho(x,x')t^{(\mathrm{k})}(x)^*. \tag{20}$$

$\left|t^{(\mathrm{k})}(x)\right|^2$ gives the probability for a particle at position x to remain in the beam and is assumed to follow poissonian statistics:

$$\left|t^{(\mathrm{k})}(x)\right|^2 = \exp\left(-n^{(\mathrm{k})}(x)\right), \tag{21}$$

where $n^{(\mathrm{k})}(x)$ is the number of absorbed photons at position x. It shows a d-periodic modulation:

$$n^{(\mathrm{k})}(x) = n_0^{(\mathrm{k})}\cos^2\left(\frac{\pi x}{d}\right). \tag{22}$$

While $\left|t^{(\mathrm{k})}(x)\right|^2$ describes a pure absorptive grating, the phase modulation of the molecular beam is described by $t^{(\mathrm{k})}(x) \propto e^{i\phi^{(\mathrm{k})}(x)}$ with

$$\phi^{(\mathrm{k})}(x) = \phi_0^{(\mathrm{k})}\cos^2\left(\frac{\pi x}{d}\right). \tag{23}$$

Here $n_0^{(\mathrm{k})}$ is the average number of absorbed photons in the antinode and $\phi_0^{(\mathrm{k})}$ is the eikonal phase, gained by integration of the interacting potential over the intensity profile of the laser. For the optical gratings they read [75]:

$$n_0^{(\mathrm{k})} = \frac{4\sigma E^{(\mathrm{k})}\lambda_{\mathrm{L}}}{hc}, \tag{24}$$

$$\phi_0^{(\mathrm{k})} = \frac{4\pi^2 E^{(\mathrm{k})}\alpha_{\mathrm{L}}}{hc}. \tag{25}$$

$E^{(\mathrm{k})}$ is the pulse energy of the laser, c denotes the speed of light, σ the absorption cross section of the particles and α_{L} is their optical polarizability for the given laser wavelength λ_{L}. Using these parameters the complex transmission function of the optical grating reads

$$t^{(\mathrm{k})}(x) = exp\left(-\frac{n^{(\mathrm{k})}(x)}{2}+i\phi^{(\mathrm{k})}(x)\right). \tag{26}$$

Transmission through a grating is described by the convolution of the Wigner function and the transmission kernel $T^{(\mathrm{k})}(x,p)$:

$$w\left(x,p\right) \rightarrow \int dp_0\; T^{(\mathrm{k})}\left(x,p-p_0\right) w(x,p_0). \tag{27}$$

For optical gratings the transmission kernel $T^{(\mathrm{k})}(x,p)$ consists of the Talbot coefficients $B_{\mathrm{n}}^{(\mathrm{k})}(x)$, gained by Fourier expansion of the transmission function $t^{(\mathrm{k})}(x)$. It is described in terms of the Bessel functions of first kind J_m:

$$T^{(\mathrm{k})}(x,p) = \frac{1}{2\pi\hbar}\sum_n exp\left(\frac{2\pi inx}{d}\right)\int ds\, exp\left(\frac{ips}{\hbar}\right) B_{\mathrm{n}}^{(\mathrm{k})}\left(\frac{s}{d}\right), \tag{28}$$

$$\begin{aligned} B_{\mathrm{n}}^{(\mathrm{k})}(\chi) = exp\left(\frac{-n_0^{(\mathrm{k})}}{2}\right)\left(\frac{\sin(\pi\chi)-\beta\cos(\pi\chi)}{\sin(\pi\chi)+\beta\cos(\pi\chi)}\right)^{\frac{n}{2}} \\ \times J_n\left(sign\left(\frac{\sin(\pi\chi)}{\beta}+\cos(\pi\chi)\right)\frac{n_0^{(\mathrm{k})}}{2\beta}\sqrt{\sin^2(\pi\chi)-\beta^2\cos^2(\pi\chi)}\right), \end{aligned} \tag{29}$$

with the dimensionless parameter:

$$\beta = \frac{n_0^{(\mathrm{k})}}{2\phi_0^{(\mathrm{k})}} = \frac{\sigma\lambda_{\mathrm{L}}}{8\pi^2\alpha_{\mathrm{L}}}. \tag{30}$$

Transformation (27) also holds for the classical case by exchanging the Talbot coefficients $B_{\mathrm{n}}^{(\mathrm{k})}(\chi)$ in (28) with the classical Talbot coefficients $C_{\mathrm{n}}^{(\mathrm{k})}(\chi)$. This can easily be done by substitution of $\sin(\pi\chi)\to\pi\chi$ and $\cos(\pi\chi)\to 1$ in (29) [53, 74]. Note that $B_{\mathrm{n}}^{(\mathrm{k})}(\chi)$ shows a periodic behavior in χ, whereas $C_{\mathrm{n}}^{(\mathrm{k})}(\chi)$ does not. For $\chi\to 0$ the coefficients are equal, $B_{\mathrm{n}}^{(\mathrm{k})}(0) = C_{\mathrm{n}}^{(\mathrm{k})}(0)$, and describe the behavior of a pure absorptive grating $\left|t^{(\mathrm{k})}(x)\right|^2$. Therefore the coefficients simplify in terms of the modified Bessel functions $I_{\mathrm{n}}(x)$:

$$B_{\mathrm{n}}^{(\mathrm{k})}(0) = (-1)^n \exp\left(-\frac{n_0^{(\mathrm{k})}}{2}\right) I_{\mathrm{n}}\left(\frac{n_0^{(\mathrm{k})}}{2}\right). \tag{31}$$

2.4.2 Beam Propagation through the TLI

The previous formalism allows to describe the beam propagation through a Talbot-Lau-Interferometer as sequences of free propagation followed by transmission through a grating. The initial beam at the first grating is assumed to be an incoherent mixture of states with a spatial extension $X_0 \gg d$ and a momentum $P_0 \gg h/d$, where h/d denotes the grating momentum kick in a semi-classical picture. The initial Wigner function at the position of the first grating $w_0(x,p_{\mathrm{x}})$ is described by the transverse momentum distribution $D(p_{\mathrm{x}})$, which is gained by integration of the three dimensional momentum density distribution $\mu(p_{\mathrm{x}},p_{\mathrm{y}},p_{\mathrm{z}})$ over two dimensions: $D(p_{\mathrm{x}}) = \int dp_{\mathrm{y}}\, dp_{\mathrm{z}}\; \mu(p_{\mathrm{x}},p_{\mathrm{y}},p_{\mathrm{z}})$. This leads to:

$$w_0(x,p_{\mathrm{x}}) = \frac{1}{X_0} D(p_{\mathrm{x}}+p_\theta), \tag{32}$$

where p_θ denotes the additional constant momentum due to a tilt. According to (27) transmission through the first grating with the transmission kernel $T^{(1)}$ leads to[9]:

$$w_1(x,p) = \frac{1}{X_0}\int dp_0\; T^{(1)}(x, p - p_0 - p_\theta)\, D(p_0 + p_\theta)\,. \tag{33}$$

With iterative usage of (19) and (27), the Wigner function transforms to $w_2(x,p)$ after free propagation for a time $t = T_1$, to $w_3(x,p)$ after transmission through the second grating and after another free propagation for a time $t = T_2$ it transforms to $w_4(x,p)$, which denotes the state of the beam before interacting with the third grating. The corresponding transformations are listed below:

$$\begin{aligned} w_2(x,p) = \frac{1}{X_0}\int dp_0\; & D(p_0 + p_\theta) \\ & \times T^{(1)}\left(x - \frac{p\,T_1}{m} + \frac{p_\theta T_1}{m} + \frac{a\,T_1^2}{2}, p - p_0 - p_\theta - a\,m\,T_1\right), \end{aligned} \tag{34}$$

$$\begin{aligned} w_3(x,p) = \frac{1}{X_0}\int dp_1 T^{(2)}(x, p - p_1) \times \int dp_0\; & D(p_0 + p_\theta) \\ & \times T^{(1)}\left(x - \frac{p_1\,T_1}{m} + \frac{p_\theta T_1}{m} + \frac{a\,T_1^2}{2}, p_1 - p_0 - p_\theta - a\,m\,T_1\right), \end{aligned} \tag{35}$$

$$\begin{aligned} w_4(x,p) = \frac{1}{X_0}\int dp_1 & \\ & \times T^{(2)}\left(x - \frac{p\,T_2}{m} + \frac{p_\theta T_2}{m} + \frac{a\,T_2^2}{2}, p - p_1 - p_\theta - a\,m\,T_2\right) \\ & \times \int dp_0\, T^{(1)}\left(x - \frac{p\,T_2}{m} - \frac{p_1\,T_1}{m} + \frac{p_\theta\,(T_1 + T_2)}{m} + \frac{a\,\left(T_1^2 + T_2^2\right)}{2},\right. \\ & \left. p_1 - p_0 - p_\theta - a\,m\,T_1\right) D(p_0 + p_\theta)\,. \end{aligned} \tag{36}$$

The third grating masks the fringe pattern of the traversing molecular beam in space. Afterwards all the molecules are detected independent of their transversal momentum p. Therefore only the spatial density distribution

[9] p_θ denotes a constant momentum. Therefore the substitution in the integral $\int dp' T^{(1)}(x, p - p') D(p')$ with $p' = p_0 + p_\theta$ leads to $dp' = d(p_0 + p_\theta) = dp_0$.

of the beam is needed, which is calculated by integrating $w_4(x,p)$ over the momentum. This leads to [53, 80]:

$$w_4(x) = \frac{1}{X_0}\sum_{k,l}\widetilde{D}\left(\frac{kT_1+lT_2}{T_T}d\right)B_k^{(1)}\left(\frac{kT_1+lT_2}{T_T}d\right)B_{l\text{-}k}^{(2)}\left(\frac{lT_2}{T_T}\right) \times \exp\left[\frac{2\pi i}{d}\left(lx - l\frac{p_\theta(T_1+T_2)}{m} + (l-k)\frac{p_\theta T_1}{m} - l\frac{a}{2}(T_1+T_2)^2 + (l-k)\frac{a}{2}T_1^2\right)\right], \quad (37)$$

where $\widetilde{D}(x)$ is the Fourier transform of the momentum distribution:

$$\widetilde{D}(x) = \int dp\, e^{-ipx/\hbar} D(p). \quad (38)$$

Due to the broad spread in momentum of the initial beam, $\widetilde{D}(x)$ is assumed to be very narrow and to peak around $\widetilde{D}(0) = 1$. So only index pairs (k,l) which fulfill $|kT_1 + lT_2| \ll T_T$ contribute to the sum in (37). In the almost resonant and symmetric approximation one assumes $T_1 = T$ and $T_2 = T + \tau$, where τ denotes a small delay of the grating timing compared to the Talbot time $|\tau| \ll T_T$. This restricts the index pairs (k,l) to $k = -l$ and changes the Wigner function $w_4(x)$ to

$$w_4(x) = \frac{1}{X_0}\sum_{l}\widetilde{D}\left(\frac{l\tau}{T_T}d\right)B_{-l}^{(1)}\left(\frac{l\tau}{T_T}d\right)B_{2l}^{(2)}\left(\frac{l(T+\tau)}{T_T}\right)\exp\left[\frac{2\pi i l}{d}\left(\Delta x'\right)\right], \quad (39)$$

$$\Delta x' = \Delta x'_s - \frac{p_\theta \tau}{m} - aT^2 - 2a\tau T - \frac{a\tau^2}{2}. \quad (40)$$

Here $\Delta x'_s$ denotes the relative grating shift of $G^{(1)}$ and $G^{(2)}$. The spatial distribution of $w_4(x)$ is scanned with the third grating, which acts as a purely absorptive grating. Therefore one can use $B_{-l}^{(3)}(0)$ from (31). For sufficiently small delays τ and due to the random phase of the impinging matter wave, $G^{(1)}$ can also be treated as a purely absorptive grating, with $B_{-l}^{(1)}(d\,l\tau/T_T) = B_{-l}^{(1)}(0)$. Convolution of (39) with the transmission Kernel $T^{(3)}(x,p)$ and integration over the whole phase space leads to the detected signal $S(\Delta x_s, \tau, T)$ behind the third grating:

$$S(\Delta x_s, T, \tau) = \sum_l S_l \exp\left[\frac{2\pi i l}{d}(\Delta x(\Delta x_s, T, \tau))\right], \quad (41)$$

$$S_l = \widetilde{D}\left(\frac{l\tau}{T_T}d\right)B_{-l}^{(1)}(0)\,B_{2l}^{(2)}\left(\frac{l(T+\tau)}{T_T}\right)B_{-l}^{(3)}(0). \quad (42)$$

As a proof for interference the periodic modulation of $S(\Delta x_\mathrm{s}, T, \tau)$ is observed by scanning over the phase of (41). This either happens by changing the grating shift[10] Δx_s, the acceleration a or the momentum p_θ. A slight delay of the third grating timing τ modulates the phase as well as the signal amplitude, due to the contribution of τ to the sharp peaked function $\widetilde{D}$. Section 2.5 further focuses on methods for scanning the spatial fringe patterns.

2.4.3 Interference Contrast

Even though a periodic modulation of the signal $S(\Delta x_\mathrm{s}, T, \tau)$ may be enough to prove the quantum behavior of molecules, it still needs a correlated value to quantify the quality of interference. Therefore this section discusses suitable measures of the matter-wave interference contrast. In a first approach, fringe shifts due to an acceleration and a tilt are neglected. The influence of a tilted beam on the fringe contrast is discussed in Section 4.
In many TLI experiments the common interference visibility from Equation (14) is used, which can be evaluated from signal minima and maxima. In case of a sinusoidal signal modulation the first order Talbot coefficients $B_{\pm 1}^{(\mathrm{k})}$ dominate over the others and determine the maximum and minimum signal. For such a case the visibility $\mathcal{V}$ is approximated by the sinusoidal visibility $\mathcal{V}_\mathrm{sin}$ [80]:

$$\mathcal{V} = \frac{S_\mathrm{max} - S_\mathrm{min}}{S_\mathrm{max} + S_\mathrm{min}} \;\rightarrow\; \mathcal{V}_\mathrm{sin} = \left| \frac{2S_1}{S_0} \right|, \tag{43}$$

which reads for the OTIMA setup:

$$\mathcal{V}_\mathrm{sin} = \left| \frac{B_{-1}^{(1)}(0)\, B_2^{(2)}\left(\frac{T+\tau}{T_\mathrm{T}}\right) B_{-1}^{(3)}(0)}{B_0^{(1)}(0)\, B_0^{(2)}(0)\, B_0^{(3)}(0)} \widetilde{D}\left(\frac{\tau}{T_\mathrm{T}} d\right) \right|. \tag{44}$$

In case of OTIMA the visibility $\mathcal{V}_\mathrm{sin}$ is a good contrast measure at weak grating laser power. For stronger power the detected signal differs from a sine due to smaller effective grating openings. Figure 4a.) shows the spatial density pattern at the position of the third grating for several grating powers, realized by different absorption numbers n_0, as described by Equation (24).

[10] In a TLI setup the overall grating shift Δx_s denotes the relative shift of all three gratings with respect to a common base $\Delta x_\mathrm{s} = \Delta x_1 - 2\Delta x_2 + \Delta x_3$.

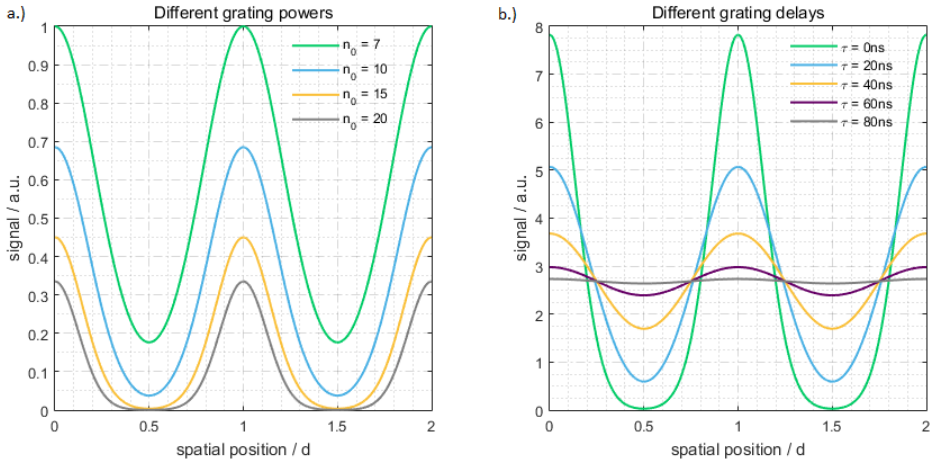

Figure 4: The spatial interference pattern at the third grating position. a.) Large grating opening fractions (low laser powers: $n_0 = 7$, $n_0 = 10$) lead to sinusoidal patterns, whereas the fringes of smaller openings ($n_0 = 15$, $n_0 = 20$) differ from a sine. b.) The spatial density patterns at the position of the third grating for a slight grating delay of τ. For $\tau = 0$ the signal shows significant modulation. For delays $\tau > 60$ ns the fringe pattern vanishes (simulation for $m = 1882$ amu and $\beta = 0.5$).

The grey and orange plot in Figure 4a.) correspond to stronger laser power, which is equivalent to a small grating opening fraction. Here $S_{\text{min}} \approx 0$ and the common visibility $\mathcal{V}$ reaches almost 100%. In such cases it is more appropriate to calculate the normalized contrast S_{N} which is not limited[11] to 100% and therefore more sensitive to disturbances in ranges where $\mathcal{V}$ is already saturated. Figure 5a.) compares S_{N}, $\mathcal{V}$ and $\mathcal{V}_{\text{sin}}$ for increasing laser power. S_{N} is defined by

$$S_{\text{N}} = \frac{S_{\text{Int}} - S_{\text{Ref}}}{S_{\text{Ref}}}. \tag{45}$$

S_{Int} represents the molecular countrate behind the third grating for resonant timing of the gratings $T = T_{\text{T}}$ and $\tau = 0$. A delay of the third grating with respect to the Talbot time resolves in barely modulated interference patterns[12], which serve as a reference measurement S_{Ref} for the contrast. Figure 4b.)

[11] Values above 100% are also possible for $\mathcal{V}_{\text{sin}}$ in case of increasing grating powers. However, this is the result of wrong approximation to a sinusoidal signal and therefore $\mathcal{V}_{\text{sin}}$ is no longer a valid measure, as shown in Figure 5 by the dotted line.

[12] The required grating delay is determined by the beam divergence of the molecular beam, which is included in $\widetilde{D}(x)$. For a large delay τ the narrow function drops. Due to (42) this also holds for the signal modulation. At OTIMA delays of $\tau = 80$ ns, corresponding to a beam divergence of $\alpha \approx 1$ mrad, had already been enough to alter the interference pattern significantly [65].

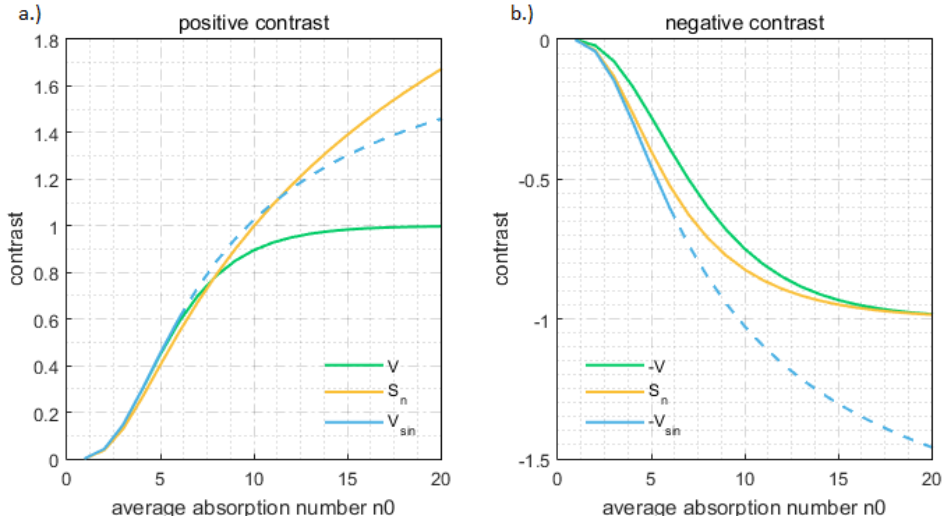

Figure 5: Contrast measures for increasing laser powers. a.) positive contrast ($\Delta x = 0$): $\mathcal{V}$ is saturated by 100 %, whereas S_N still increases. b.) negative contrast ($\Delta x = d/2$): The normalized contrast shows the same behavior as the negative visibility $-\mathcal{V}$. For both plots the dotted line marks the range where $\mathcal{V}_\mathrm{sin}$ is no longer a valid approximation of the visibility (simulation for $m = 1882$ amu and $\beta = 0.5$).

illustrates the spatial interference pattern at the position of $G^{(3)}$ for different grating delays τ, which correspond to a distance of $L = L_\mathrm{T} + v\tau$ from the second grating. A symmetric pulse separation ($\tau = 0$) shows stronger spatial modulation than an asymmetric pulse separation due to a delay $\tau \neq 0$. In case of $\tau = 80\,\mathrm{ns}$ (grey line) the pattern is almost constant and therefore serves as a reference signal.
The normalized contrast S_N can therefore be detected by a simple change of the pulse separation. This avoids translation of the third grating to detect the interference contrast, but still the contrast depends on the overall grating shift Δx_s. A shift of the gratings due to misalignment alters the contrast and could also lead to negative values of S_N. This is the case for $\Delta x_\mathrm{s} = d/2$, where S_N. Figure 5b.) shows $-\mathcal{V}$ and S_N for minimal (negative) contrast, where both values show almost the same behavior with a saturation[13] at $S_\mathrm{N} = -\mathcal{V} = -1$.

[13] For easier comparison of the behavior of the normalized contrast S_N Figure 5b.) shows $-\mathcal{V}$ and $-\mathcal{V}_\mathrm{sin}$, even though they cannot be negative due to their definition.

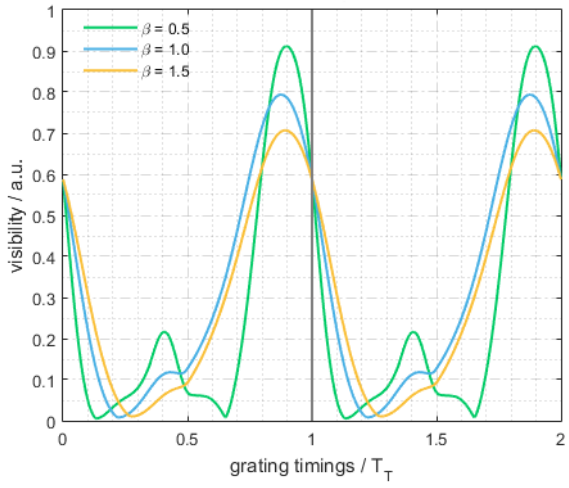

Figure 6: Periodic modulation of the fringe visibility $\mathcal{V}$ for symmetric variation of the grating pulse separation. The resonances are narrower for smaller β values. At multiples of the Talbot time $T = n\ T_\mathrm{T}$ the visibility for all β values is the same due to the pure absorptive behavior of the second grating (simulation for $m = 1882$ amu and $n_0^{(\mathrm{k})} = 6$).

Similar to the spatial Talbot carpet one can observe a periodic modulation of the contrast in the time domain. The grating pulse separation T is scanned symmetrically for the three grating setup with $T = T_3 - T_2 = T_2 - T_1$. Here T_k ($k \in \{1, 2, 3\}$) is the timing of grating $G^{(\mathrm{k})}$. This is shown in Figure 6 for three different β values. The grating power $n_0^{(\mathrm{i})}$ is fixed for all gratings. Therefore different β values represent different optical polarizabilities α_L of the particles, see Equation (30).
All three graphs show a periodic reappearance of the contrast at integers and fractions of the Talbot time. All resonances show their maximum at a pulse separation of $T < T_\mathrm{T}$. For larger polarizabilities (green line $\beta = 0.5$) the peaks are narrower and the fractional Talbot order resonances are more pronounced[14]. For $T = T_\mathrm{T}$ (marked by the vertical line) all three graphs show the same visibility. Here the second grating acts as a pure absorptive grating, independent of the particle polarizability, because $B_\mathrm{n}^{(2)}(T/T_\mathrm{T}) = B_\mathrm{n}^{(2)}(1) = B_\mathrm{n}^{(2)}(0)$ (see Equations (29) and (31)).

[14]The simulations use the theoretical visibility $\mathcal{V}$. Differences to the normalized contrast, including the beam divergence are discussed in Chapter 4.

2.5 Quantum or Classical Contrast?

The occurrence of a d-periodic fringe pattern behind the second grating is not necessarily a proof for the quantummechanical delocalization of the molecules. It might also be described by classical theories. Here the molecules are treated as particles which follow ballistic trajectories through the interferometer. This also creates fringe patterns at the position of the third grating. Some deflectometers even used those Moiré-type shadow patterns to show the equivalence principle for atoms [81] or antimatter [82].
In the chosen mathematical frame of the TLI setup the classical patterns can easily be obtained by exchanging the Talbot coefficients $B_{\mathrm{n}}^{(\mathrm{k})}(\chi)$ by the classical coefficients $C_{\mathrm{n}}^{(\mathrm{k})}(\chi)$. Even though they are identical for $\chi \to 0$, they clearly differ for an increasing pulse separation T. Whilst $B_{\mathrm{n}}^{(\mathrm{k})}(\chi)$ reveals a periodic behavior $C_{\mathrm{n}}^{(\mathrm{k})}(\chi)$ does not oscillate with $\chi = dT/T_{\mathrm{T}}$. A scan over one Talbot order would therefore be sufficient to clearly distinguish between quantum and classic behavior, as shown in Figure 7. The quantum visibility shows clear resonances close to integers of the Talbot time, while the classical visibility shows different behavior for increasing pulse separation. However, a scan over the Talbot carpet either requires a variable length of

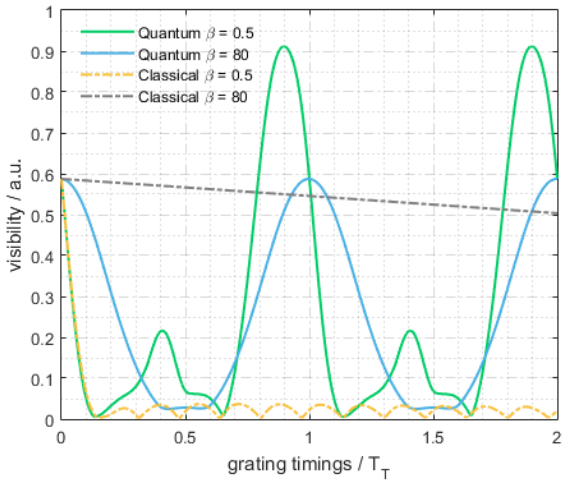

Figure 7: The differences between classical and quantum fringe patterns for a symmetric scan of the pulse separation time. For low values of β (e.g. $\beta = 0.5$) the classic contrast is significantly smaller than the quantum contrast and shows another modulation. For higher values of β the classical contrast in the surrounding of the first Talbot order is much higher. A single measurement is not sufficient to differ between quantum and classical behavior (simulation for $m = 1882$ amu and $n_0^{(\mathrm{k})} = 6$).

the interferometer or a broad velocity distribution of the particle beam[15]. Both are hard to achieve in the OTIMA setup. If the beam contains molecular clusters one could also scan the Talbot carpet for fractions and integer multiples[16] of T_{T}. Still one could doubt the quantum behavior and explain those observations with classical trajectories of particle which change their values of β for different clusters or velocities.
If the particle properties are known and the TLI is well characterized one single measurement is sufficient to distinguish between the quantum and classical pattern just by comparison with the theoretical visibility values. Without knowledge of β a single measurement is not sufficient to prove the quantum behavior, as shown in Figure 7. For $\beta = 80$ the classical visibility (dotted grey line) reaches values of $50\% - 55\%$ close to the Talbot time and could therefore be misinterpreted as quantum contrast. In this case a second measurement with a shorter grating pulse separation allows for a distinction. While the quantum contrast decreases for sufficient delay of the grating timing[17], the classical contrast still increases.

One could also use the dependence of the visibility on the grating power to confirm the quantum model. This requires two power scans with different pulse separation, as shown in Figure 8. For a grating pulse separation time of $T = T_{\mathrm{T}}$ the second grating acts as a pure absorptive grating and the quantum visibility increases with the grating power, as also shown in 6a). The classical visibility mimics this behavior only for high values of $\beta \gg 1$. For pulse separation of $T \neq T_{\mathrm{T}}$, as shown in Figure 8b.), the phase modulation of the second grating contributes to the quantum visibility and causes a local maximum. This maximum cannot be described in terms of the classical model with the high $\beta = 80$ from the first measurement in Figure 8a.).
Another way to clearly distinguish between quantum and classical behavior is the observation of the fringe periodicity for fractional Talbot orders. While the quantum interference fringe of a symmetric TLI shows a period of d for $T = T_{\mathrm{T}}$ and $d/2$ for $T = T_{\mathrm{T}}/2$, the classical shadow remains with a period of d [75, 76]. Therefore detection of the spatial interference pattern for fractional Talbot orders is a valid tool to prove the quantum model. Due to the lower contrast of the fractional Talbot orders this is still an outstanding challenge for OTIMA.

[15] The former enables interaction of particles with the gratings independent of their spatial position within a time of $2T$. The latter guarantees sufficient overlap of a broad particle cloud with the gratings, such that detection of particles for each pulse separation T at fixed grating positions is possible.

[16] The Talbot time T_{T} scales linearly with its mass m. For a mass $m' = 2m$ the time T_{T} corresponds to the fractional Talbot order of $1/2$ of m' and vice versa.

[17] This depends on the β value of the molecules, since it influences the width of the visibility resonance. Corresponding to Figure 6a.) delays of $0.25\ T_{\mathrm{T}}$ should be a good choice.

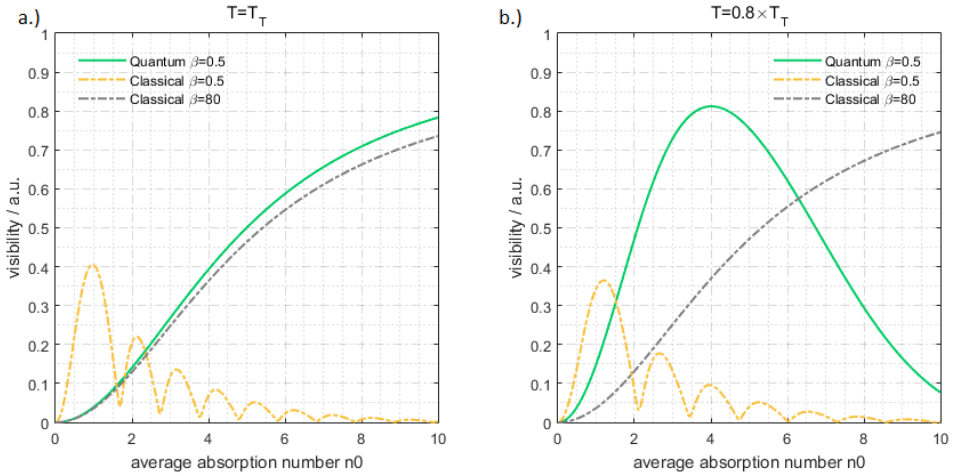

Figure 8: Two power runs to distinguish between quantum and classical fringe patterns. The first measurement a.) uses a grating pulse separation of $T = T_{\mathrm{T}}$, which restricts the second grating to a pure absorptive behavior. This leads to an increase of the visibility $\mathcal{V}$ for higher laser power. To mimic this behavior in a classical picture the particles require high values of $\beta \gg 1$, for example $\beta = 80$. In b.) the pulse separation is set to $T = 0.8 \times T_{\mathrm{T}}$. Now $G^{(2)}$ also modulates the phase which causes a local maximum of the visibility. This cannot be achieved by classical effects with $\beta = 80$ (simulation for $m = 1882$ amu and $n_0^{(\mathrm{k})} = 6$).

Detection of the grating period for integer Talbot orders has been done by slightly tilting the second grating laser [65] or tilting the molecular beam [83], where the latter is further discussed in Chapter 4. Another method relies on local heating of the interferometer mirror at the reflection area of one grating laser[18]. The thermal expansion of the mirror surface causes an overall grating shift Δx_{s} and enables a scan of the spatial interference pattern [76].

[18] It is favorable to choose the area of $G^{(2)}$ because its grating shift contributes stronger to the overall grating shift Δx_{s} than a shift of the other gratings.

3 Experimental Setup

A basic representation of the experiment is shown in Figure 9. It contains the molecular beam source, the interferometer and the detector. They are housed in two different vacuum chambers: The source chamber (SC) houses the molecular source. It is pumped by two molecular pumps[19] with a pumping speed of 685 l/s for N_2. This allows a background pressure down to 10^{-8} mbar. A differential pumping stage with two pumps[20] connects the source to the main chamber (MC). A skimmer inside the pumping stage separates the high pressure source side from the low pressure main chamber. The main chamber is pumped by three molecular pumps delivering a background pressure down to 2×10^{-9} mbar, required to avoid collisional decoherence [84]. For an even lower pressure a baffle, mounted inside the MC, may be cooled with liquid nitrogen. The optics chamber (OC), a third vacuum chamber containing all optics for guiding and shaping of the grating laser beams, is connected to the source chamber through a window.
Laser desorption from a carbon wheel injects molecules into a directed supersonic beam. The beam is shaped by a conical skimmer and further collimated by two orthogonally oriented slits. The rectangular shaped molecular beam is guided through the interferometer, where it passes three standing waves

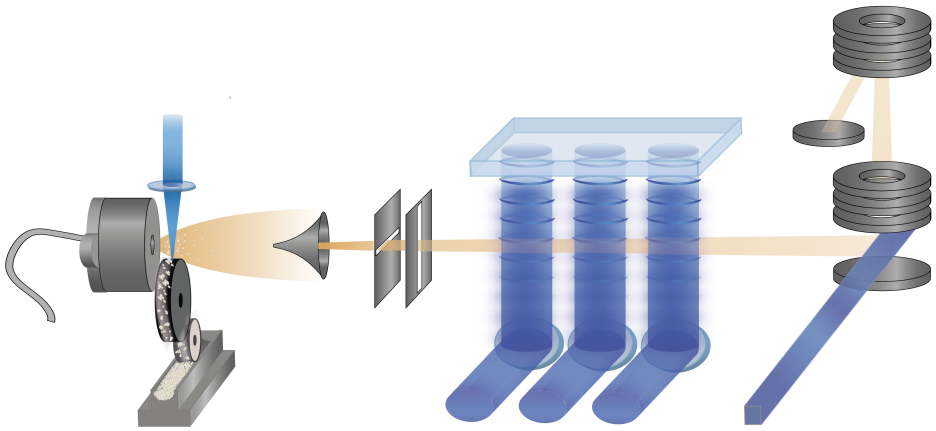

Figure 9: The OTIMA setup used for this thesis: Laser desorption injects the molecules into a supersonic expansion. The molecular beam is shaped by a skimmer and two collimators before it enters the interferometer. This consists of three standing light waves formed by retro-reflection of F_2 laser beams ($\lambda_L = 157\,\text{nm}$) on a single mirror. Ionization by a running wave and time-of-flight mass spectrometry detects the particles.

[19] Pfeiffer, HiPace 700
[20] Pfeiffer, HiPace 700 and HiPace 300

formed by retro-reflected F_2 laser beams ($\lambda_L = 157\,nm$) on a single mirror. An electrode close to the mirror surface removes ionized particles from the molecular beam axis. Even if photofragmentation is the dominant relaxation process after absorption of a 157 nm photon, the geometrical arrangement of the experiment ensures beam depletion since photofragmentation is typically much faster than the experimental timescale. The spatially intensity modulated particle beam is ionized by the running wave of a fourth F_2 laser [21] and detected with a time-of-flight mass spectrometer (ToF-MS)[22].
Operation in the time domain requires accurate precision of grating timing. A pulse generator[23] triggers the source, the lasers and the ToF-MS. GaP-photodiodes monitor the laser timing and provide a feedback loop controlled by a homebuilt software package: Molecular Optics Programming System (M.O.P.S.) [77]. The feedback loop allows it to monitor and correct the actual grating laser timings.
The experiment runs at 100 Hz and sends one data frame for each run to the software. Each of the frames includes the timing of the grating lasers and the recorded mass spectrum. A typical measurement contains about

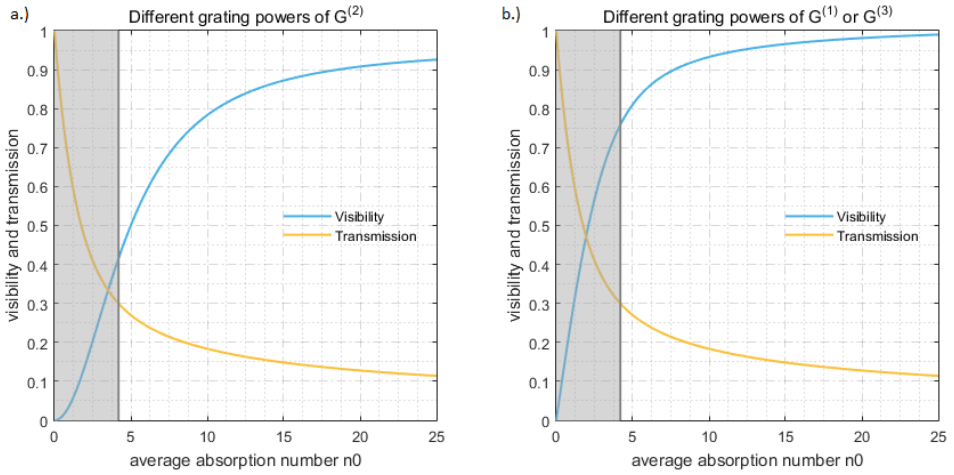

Figure 10: The influence of the grating power on the visibility and the transmission through the gratings. a.) Variable grating power of $G^{(2)}$ and b.) variable grating power of $G^{(1)}$ and $G^{(3)}$. High visibility values are gained for low transmission rates at the expense of molecular flux. The grey bar marks the area with transmission rates above 30%. This section shows low visibility values. Transmission rates between $20\% - 30\%$ have proven to be a good compromise for measurements.

[21] Coherent, ExciStar XS 500, SA-base, SSXS, with purge/E-mon
[22] Stefan Kaesdorf, RFT50
[23] BNC, model 575 pulse/delay generator

5000 frames. To measure the normalized contrast, as described in Section 2.4.3, the measurement switches between two modes: The interference and the reference mode. The interference mode uses a symmetric pulse separations $T_2 - T_1 = T_3 - T_2$, whereas the reference mode adds a slight delay τ such that $T_2 - T_1 = T_3 - T_2 + \tau$. The required delay is determined by the molecular beam divergence, as described in Section 4.1. Integration over the detected mass intensities of a chosen peak yields the values of S_{Int} and S_{Ref} to further calculate the normalized interference contrast with Equation (45). Each measurement ends with the detection of the grating transmission rate. Values between $20\% - 30\%$ have proven to be an ideal tradeoff between signal intensity and contrast, as shown in Figure 10. Here transmission rates below 30% yield visibilities above 40%.

3.1 Molecular Source

A molecular beam source needs to fulfill several criteria to fit the requirements of OTIMA. The source needs to be pulsed to guarantee detection of only those particles, which have interacted with all three pulsed gratings. If the pulse lengths are too long, some particles may have not interacted with all three gratings. The molecular velocity is limited by the geometrical arrangement of the interferometer, where two gratings are separated no more than $\Delta x = 2\,\mathrm{cm}$. At least one Talbot time must fit between two gratings, which gives an upper bound of $v \leq \Delta x / T_{\mathrm{T}} = h\Delta x/(md^2)$. A lower bound is given by the coherence length of the grating lasers, which restricts molecules to travel through the interferometer before the gravitational fringe shift reaches values of around 5 mm. To prevent decoherence caused by thermal radiation [17], the source mechanism needs to allow for sufficient cooling of the molecular internal degrees of freedom.
Figure 9 shows a sketch of the molecular beam source. It consists of a sample slide, a valve which produces a supersonic noble gas beams and a laser for desorption from the target. Gramicidin is filled into the sample slide as powder, where a rotating felt wheel picks up the sample and coats a carbon wheel. A lens focuses the laser pulse of a diode pumped optical parametric oscillator[24] onto the carbon wheel. Soft desorption removes the molecules and inserts them into a supersonic beam, produced by an Even-Lavie valve. The valve is placed about 2 mm above the wheel. The source and the laser are both pulsed and the supersonic expansion delivers cooling and velocities suited for the requirements of OTIMA.

[24] Ekspla, NT242A-HE-100-SH/SFG

3.1.1 Gramicidin D

In this thesis Gramicidin D is used for interference measurements. It is a mixture of Gramicidin A, B and C. These peptide antibiotics consist of 15 amino acids and differ by one position in their chain-sequence[25], where A contains Tryptophan, B Phenylalanin and C Tyrosin. Another subdivision into two groups is given by the first position of the chain, where $X1$ is attached to Valin and $X2$ to Isocleucin[26]. The six types of Gramicidin differ in mass by less than 60 amu. Figure 11 shows the composition of the Gramicidin sample used in the measurements, where Gramicidin $A1$ reveals the highest intensity[27].
In Gramicidin the amino acids occur alternatingly in L and D conformation, which permits the molecule to form a β-strand structure. The β-strand is a regular structure in proteins which allows connection with other strands via hydrogen bonds.

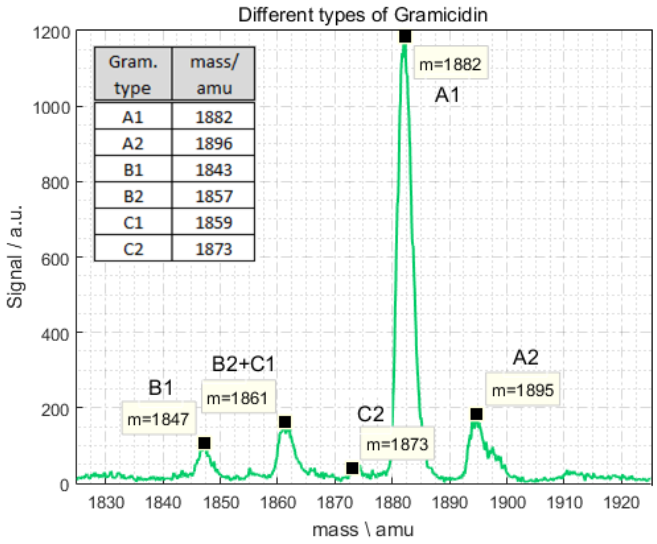

Figure 11: A mass spectrum of the Gramicidin D sample used in the measurements shows highest intensities for Gramicidin $A1$. Five out of the six different types are resolved. Only $B2$ and $C1$ are not clearly distinguishable due to the mass difference of 2 amu.

[25] For Gramicidin D it is: Formyl – L – Val_1 – D – Gly_2 – L – Ala_3 – D – Leu_4 – L– Ala_5 – D – Val_6 – L – Val_7 – D – Val_8 – L – Trp_9 – D – Leu_{10} – XXX_{11} – D – Leu_{12}– L – Trp_{13} – D – Leu_{14} – L – Trp_{15} – Ethanolamine. XXX denotes the position of Tryptophan, Phenylalanin or Tyrosin.

[26] X stands for Gramicidin type A, B or C.

[27] The experimental setup to detect such a mass spectrum is presented in Chapter 3.4.

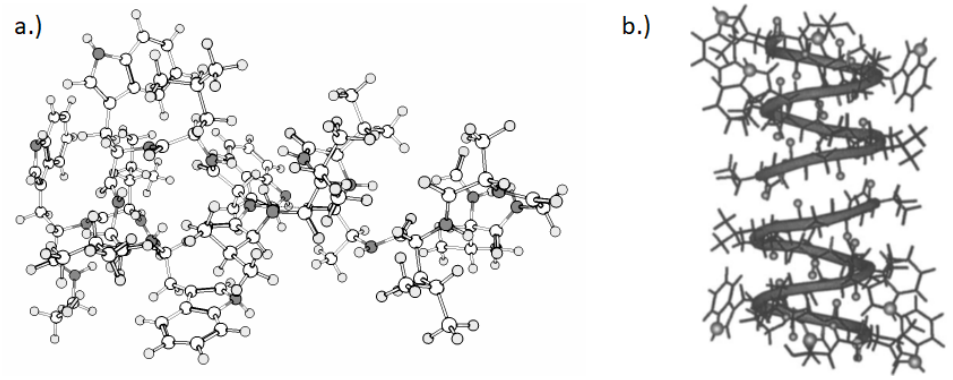

Figure 12: The structure of Gramicidin $A1$. a.) The molecular structure of a single Gramicidin molecule with the structural formula $C_{99}H_{140}N_{20}O_{17}$ and a mass of $m = 1882$ amu (plotted with ChemDraw). b.) Two Gramicidin molecules can form a helix due to the alternating sequence of L- and D-amino acids of Gramicidin. Therefore it also serves as an ion channel in cells, where b.) is taken from [85].

In case of Gramicidin this enhances the formation of a helix [85] consisting of at least two Gramicidin molecules. Figure 12b.)shows an example of such a helix. This structure allows Gramicidin to act as an ion channel in organic cells [86].

3.1.2 Source Preparation

The sample unit needs to provide a homogeneous coating of the carbon wheel to create a stable molecular beam of constant intensity and low pulse-to-pulse fluctuations. Double-ablation of the laser from the same spot is prevented by the chosen wheel frequency of 1 Hz. With a diameter of $d = 30$ mm and a laser frequency of 100 Hz the carbon wheel moves by $\Delta s = \omega r \Delta t \approx 900$ μm from shot to shot, which is almost by a factor of 10 larger than the laser beam diameter.
Creating a homogeneous coating, stable over several hours, appeared to be a tough challenge. It took several steps in order to iterativley approach the final version. In the first setup a sample slide coated the felt wheel as shown in Figure 13a.). The laser was focused to a diameter of 5 mm with an energy of 10 mJ per shot. The thickness of the coating was manipulated by changing the speed of the translation stage. For interference measurements the sample slide had to translate with high speed to gain a high enough molecular signal. This limited the signal to half an hour. After a very short time, the whole source chamber and the UV optics were coated with a thick layer of molecular sample. A collision-cell, which is conventionally used

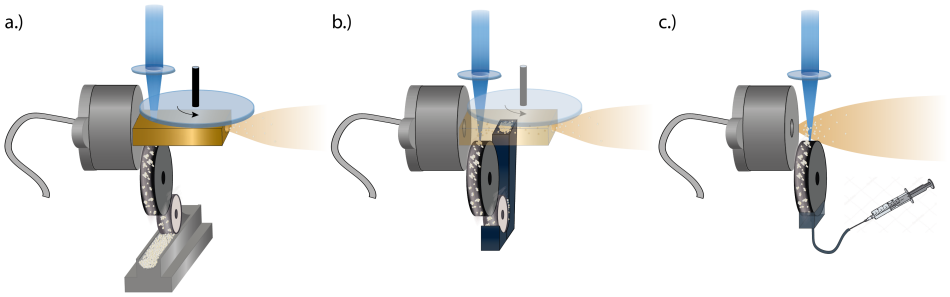

Figure 13: The tested sample supply mechanism of the source. a.) The felt wheel is coated with a translational sample slide. Even though this setup delivers sufficient molecule intensities, measurements are limited to 30 minutes due to the high waste of sample. To protect the optics from coating a collision-cell and a rotating glass-slide were used. Desorption with a fs- instead of a ns-laser pulse reduced the coating and made the rotating glass slide dispensable. b.) A funnel in contact with the felt wheel delivers homogeneous coating for two hours, but blocking of the funnel resulted in low reliability. c.) A solved molecular sample coats the carbon wheel from a bowl, supplied with a capillary. This setup reduces the waste of sample and its proof of principle already succeeded.

to enhance molecular clustering, was mounted to shield the optics and the chamber from such layers. An additional rotating glass-slide was mounted above the collision-cell to cover the laser entrance and strip off coating of the glass-slide itself.
To further improve the coating and account for the required fast recoating of the wheel, setup 13b.) used a tailored 3D-printed funnel instead of the sample slide. This led to stable signals lasting up to two hours. However, frequently the powder got stuck inside the funnel. Stirring motors and additives like Aerosil (used as anticaking and free-flow agent) improved the reliability of the source, but the large amount of material needed was still limiting the efficiency of measurements.
For measurements with Gramicidin within this thesis the setup from Figure 13a.) is used. Due to the low particle detection rate, the high waste of material and the coating of the source chamber, the assumption reinforced that laser desorption is followed by phase explosions and spallation (further described in Section 3.1.4). Therefore the laser pulse energy is reduced below 1 mJ to prevent bigger chunks of flakes beside the desired single molecules. Several tests to increase efficiency showed that pre-preparation of the sample powder can significantly improve the signal count rates. A powder of Gramicidin is solved in a mixture of Acetone and water (95:5 Vol%). The solvent is subsequelty removed until a powder remains which increases the signal in-

tensities. For calibration purposes Tetraphenylporphyrin (TPP) with a mass of 615 amu is added to Gramicidin with a ratio of 1:40.

Figure 13c.) shows the schematic of a liquid source, which was also tested. The molecules are solved in pure or mixed solvents and pumped through a capillary to a bowl below the carbon wheel. After contact with the bowl the solvent on the carbon wheel evaporates and a homogeneous coating remains. The proof-of-principle experiment already succeeded. The volatility of the molecules increased and therefore also the desorption efficiency. Due to its low waste of material it seems to be a good candidate for future measurements with tailor made or expensive molecules available in small amounts. Such a liquid based source is currently under construction and will be tested soon.

3.1.3 Even-Lavie Valve

An Even-Lavie valve is used to create a supersonic atomic beam. The valve consists of a high pressure reservoir connected to a conical expansion nozzle with a diameter of 100 μm. A magnetic plunger seals the high pressure reservoir (typical values up to 40 bar), limits the opening widths to maximal 25 μs and ensures sharp pulses without ringing effects up to repetition rates of 550 Hz [87].
The valve opening widths Δt_v and the pressure of the carrier gas p_0 are two parameters which are varied to optimize the detected signal while accordingly adjusting ToF-MS and detection timing. Argon is used as carrier gas for all measurements in this thesis. It allowed the production of highest signal intensities under the given experimental parameters, with $\Delta t_\mathrm{v} = 21.5\,\mu$s and $p_0 = 22\,$bar. For an initial temperature of $T_0 = 300\,$K and a heat capacity of $C_\mathrm{p} = 5/2\ k_\mathrm{B}$ the maximum velocity of Argon is given by:

$$v_\mathrm{Ar,max} = \sqrt{\frac{2 \times 300\ \mathrm{K} \times 5/2 k_\mathrm{B}}{40\,\mathrm{amu}}} \approx 560\ \frac{\mathrm{m}}{\mathrm{s}}. \tag{46}$$

For maximal accelerated Gramicidin with a velocity equal to the co-expanding argon atoms the particles are assumed to move about 1.6 cm within one Talbot time ($T_\mathrm{T,Gram} = 29.1\,\mu$s). This is compatible with the grating arrangement on the interferometer mirror.
Due to the low background pressure in the source chamber, with $p_\mathrm{B} = 2 \times 10^{-7}\,$mbar, the distance between the nozzle and the the Mach disk x_M is given by:

$$x_\mathrm{M} = 0.67 \times 100\ \mu\mathrm{m} \sqrt{\frac{22\,\mathrm{bar}}{2 \times 10^{-7}\,\mathrm{mbar}}} \approx 22\,\mathrm{m}. \tag{47}$$

For high repetition rates the pumping speed is may not sufficient to hold a background pressure of $2 \times 10^{-7}\,$mbar, but even a pressure of $p_\mathrm{B} = 10^{-5}\,$mbar

yields a distance of 3 m which exceeds the length of the experimental setup. Therefore insertion of a skimmer in a distance of 0.5 m to the nozzle guarantees beam shaping in a shock wave free environment. This is in good agreement with [87], whereupon shock waves can be neglected for pressures below 10^{-5} mbar.

3.1.4 Desorption Laser

A diode pumped optical parametric oscillator OPO[28] is used to desorb molecules from the glassy carbon wheel. The laser has a tuning range from $225\,\text{nm} - 2.6\mu\text{m}$ and a pulse duration of ~ 4 ns. It is pumped by the third harmonic of a diode pumped Nd:YAG (355 nm) laser with 41 mJ pulse energy and a maximum conversion efficiency of approximately 15 %, a beam divergence below 3 mrad and a beam diameter of 5 mm.
Instead of the pump output, the molecular source uses the tuneable output at a wavelength of 355 nm, which restricts the laser pulse energy to 3 mJ. A polarizing beamsplitter (PBS) is further used to attenuate the pulse energy to below 1 mJ.
The desorption process is triggered by the focused laser. This creates a plasma on the surface of the carbon wheel and the visible ablation of the target begins. The material heats up, melts and, in case of sufficient energy transfer, vaporizes [88]. Therefore desorption of single molecules from the surface occurs usually simultaneously with "phase explosion" and "spallation" [89]. Phase explosion describes ejection of small amounts of melted, liquid droplets, which may still vaporize to single molecules, depending on their stored energy. Spallation denotes chunks ejected by laser induced shockwaves, which do not vaporize. This fits to the chunk observations mentioned in Chapter 3.1.2. Referring to [88], a decrease of the laser pulse length at equal energy to sub-pico seconds increases the laser field strength and drives the electrons to much higher temperatures. Subsequent equilibration transfers more heat to the ions, which undergo a faster transition through the melt phase. This results in a higher fraction of vaporized molecules. In [90–92] it is stated, that intensities of 10^{13} W/cm^2 are sufficient to desorb amphiphilic lipids, hydrophobic proteins and intact biomolecules up to masses of 45 kDa for wavelengths of 800 nm. Here single photon absorption is not enough to ionize the molecules, whereas the high intensity enhances nonlinear processes like multiphoton-absorption. Due to the shorter laser-target interaction time the heat-affected area is much smaller and stays within the focal volume [93]. So in a second attempt, a femto-second laser[29] with a fundamental wavelength of 1030 nm and tuneable pulselengths between 290 fs and 10 ps was coupled to the source. A harmonic generator delivered wavelengths of 343 nm with pulse energies of 40 μJ and an energy stability of 0.5% over 24 hours.

[28] Ekspla, NT242A-HE-100-SH/SFG
[29] Topag, Carbide-4W

The laser beam, with a diameter of 3 mm, was focused to a 50 μm spot on the carbon wheel, to guarantee intensities of $I \approx 10^{13}\,\mathrm{W/cm^2}$.

3.2 VUV-Lasers

The chosen laser wavelength of $\lambda_\mathrm{L} = 157\,\mathrm{nm}$ delivers a photon energy of 7.9 eV and a grating period of d=78.8 nm. Therefore OTIMA, with the Talbot time of T_T =15 ns/amu, fits to a broad range of masses and nanoparticles, since the photon energy exceeds the ionization energy of many organic molecules and clusters.
In the current OTIMA setup the optical gratings are realized from three identical discharge pumped Fluorine lasers[30]. The active medium consists of excited fluorine dimers (0.2 vol%) in a helium buffer gas (99.8 Vol%). Lasing between two bound electronic states [94] results in narrow emission lines. For the most pronounced lines at 157.63 nm and 157.52 nm, where the first is about five times stronger than the second, the FWHM linewidth is about 0.85 pm [95]. This gives a longitudinal coherence length of $\Lambda_\mathrm{coh}^\mathrm{long} \approx \frac{\lambda^2}{\Delta\lambda} = 2.9\,\mathrm{cm}$. Therefore the formation of proper standing waves is restricted to a small region close to the interferometer mirror and the molecular beam needs to traverse close to the mirror surface. To protect the mirror from coating the minimum distance in a typical measurement is about 100 μm, while the particle cloud usually extends over 1 mm along the standing wave. The laser beam profile at the outcoupler has a rectangular shape [3 mm × 9 mm] with a Gaussian intensity distribution along both axes. With a divergence of [0.8 mrad × 1.6 mrad] the beam has a transverse coherence length $\Lambda_\mathrm{coh}^\mathrm{trans} \approx \frac{\lambda R}{2}\,[0.8\,\mathrm{mrad} \times 1.6\,\mathrm{mrad}] = [13\,\mu\mathrm{m} \times 30\,\mu\mathrm{m}]$ at the mirror surface in a distance of R =1.5 m. Since the center wavelength of the Fluorine lasers is stable within one linewidth for cavity differences in temperature or gas pressure, it is possible to realize the gratings with three physically independent lasers.
The laser pulse lengths are about $\tau = 10\,\mathrm{ns}$ at repetition rates up to 250 Hz and a jitter below 5 ns, where the low jitter is crucial for operation in the time-domain. The operation energy is specified with 4 mJ at a shot to shot energy stability of 20 %. Due to the high absorption cross section of oxygen at wavelengths of $\lambda_\mathrm{L} = 157\,\mathrm{nm}$ [96] the beam lines need to be evacuated. A pressure of 10^{-4} mbar is sufficient to neglect energy losses during propagation to the interferometer mirror in a distance of 1.5 m. Purging the beam lines with air allows for continuous attenuation of the pulse energies. In addition the central grating laser may be attenuated by filling a cell with air, which is inserted into the second beam line.

[30] GAM, EX50

3.3 Calcium Fluoride Optics and Laser Alignment

Only a few materials are capable to serve as optics for wavelengths of $\lambda_L = 157\,\text{nm}$. At OTIMA calcium fluoride (CaF_2) optics are used for the mirrors, lenses and windows. The high reflectance (HR) CaF_2 mirrors show reflectivities up to $\mathcal{R} = 95\,\%$, whereas the windows showed variances from $70 - 95\,\%$ in transmission [75].
Each of the grating beams is guided by four CaF_2 mirrors through the optic box and is focused with a cylindrical lense to a spot about 1 cm behind the interferometer mirror. This results in a beam waist of approximately $1 \times 10\,\text{mm}$ on the mirror surface. The optics absorb some of the 157 nm radiation [97] and emit blue fluorescence light. With a CCD camera[31] the fluorescence on the window between the main chamber and the optic box plus the interferometer mirror are captured and used for alignment purposes. Overlapping of those two spots with help of two motorized mirrors allows in situ alignment of the optical gratings. To reduce contamination of the optics by cracked hydrocarbons, resulting in a brownish surface deposition [98], the whole optic box is floated with nitrogen at a constant pressure of 1 mbar[32]. The interferometer mirror has a rectangular shape of [7cm × 4cm] and was specially produced to fit the requirements of a smooth and flat surface. Deformations along the reflection area of the laser spot need to be kept below 5-10 nm [99], otherwise particles along the molecular beam will experience differently shifted interferometers, which washes out the interference pattern. Figure 14 shows the mirror roughness of the current interferometer

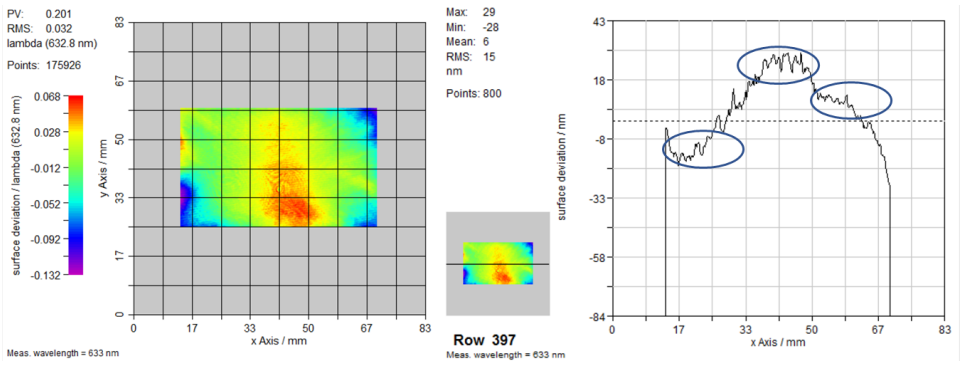

Figure 14: Surface roughness of the interferometer mirror. Even though the mirror shows a rough modulation in beam direction the marked spots are smooth enough to form proper light gratings. The overall phase shift almost cancels out, but $\Delta x_s \approx 0.23\,d$ is still enough to alter the interference contrast (coated and measured by Laseroptik Garbsen).

[31] Spiricon, SP620U
[32] In contrast to oxygen, nitrogen does not absorb the VUV-photons.

mirror. Even though the coating shows deviations of $\Delta x = 50\,\mathrm{nm}$ along the beam propagation axis, the mirror is sufficiently flat within the marked laser-mirror-interaction areas. The overall phase shift, in absence of external forces and tilts of the beam is given by $\Delta x_\mathrm{s} = \Delta x_1 - 2\Delta x_2 + \Delta x_3 \approx 18\,\mathrm{nm} = 0.23\,d$. This needs to be taken into account for calculations, since it may alters the maximum contrast as described in Chapter 2.4.3.

3.4 Time-of-Flight Mass Spectrometry and Data Analysis

To detect the ionized particles an othogonal reflectron ToF-MS is used. It operates with two acceleration stages in a Wiley McLaren mode [100] and a triple stack micro channel plate (MCP). An analog-to-digital converter with a time resolution of 1 ns sends the spectra to a computer, which collects and averages all frames of the same measurement mode. Each frame contains a spectrum of signal intensities in dependence of the molecular flight time, which first needs to be calibrated. In a simple picture one can calibrate the mass spectra with one known mass[33] m_c. For equal kinetic energies $E_\mathrm{kin} = m_\mathrm{i} L^2/2(T_\mathrm{i} - t_0)^2$ of all masses m_i along the same distance L with the same starting point[34] t_0, the mass spectrum transforms like:

$$m_\mathrm{i} = m_\mathrm{c} \frac{(T_\mathrm{i} - t_0)^2}{(T_\mathrm{c} - t_0)^2}, \tag{48}$$

where T_i and T_c denote the flight time of m_i and m_c. This is a good approximation for the local surrounding of the calibration mass.
To calculate the normalized contrast with Equation (45) the mass spectra intensities within the range of a few amu[35] are summed up and subtracted from the background, to gain S_Int and S_Ref. The background is calculated by summing up intensities within an area in front of the peak. The assumption of proportionality between the mass spectrometer amplitudes and the number of impinging molecules causes a systematic error, because the amplitudes may also depend on the impact point on the MCP and the particle velocity.
This is taken into account within the error estimations. They assume a maximum of one impinging particle per frame and therefore act as some kind of "worst case scenario". The software compares each amplitude of the spectra with a threshold, which is calculated with the standard deviation of the background noise. This delivers a sequence of zeros and ones. The

[33] More accurate calibration methods rely on regression analysis through several points of the spectrum.

[34] t_0 is either represented by the timing of the ionization laser or by the timing of the electric field, whichever comes first. In the current setup it is the timing of the ionization laser.

[35] A few amu are usually enough to cover the molecules full mass distribution due to the isotopic spread of its atoms.

probability of not detecting a particle P_{zero} is assumed to follow Poissonian statistics:

$$P_{\text{zero}} = 1 - N_{\text{event}}/N_{\text{frames}}, \tag{49}$$

$$P_{\text{zero}} = e^{-\lambda}, \tag{50}$$

with λ being the average number of particle counts per frame. The total number of detected molecules N within one measurement is given by:

$$N = -N_{\text{frames}} \times \ln\left(P_{\text{zero}}\right). \tag{51}$$

The standard deviation of $\sqrt{N}$ is used as statistical error for S_{Int} and S_{Ref}. Gaussian error propagation delivers the 1σ error-bars of the analysis.

4 Simulations

The simulations presented in this chapter differ from the previously discussed calculations in two points. First of all they use the normalized contrast S_{N} instead of the visibility $\mathcal{V}$ to quantify the interference fringes. Therefore they consider the transverse momentum distribution of the molecular beam $D(p)$, which reduces the interference contrast for asymmetric grating delays. Secondly, the modulation due to a slight tilt of the molecular beam is considered. Together the adaptions allow more precise and reliable simulation of experimental results in terms of resonance curves[36].
If not specifically mentioned all simulations in this chapter are run on Gramicidin $A1$ with a mass of 1882 amu and assume a beam divergence of $\alpha = 1$ mrad, $\beta = 0.5$, an average photon absorption number of $n_0^{(\mathrm{k})} = 6$ and grating delays in the reference and interference mode of $\tau_{\mathrm{Ref}} = 100$ ns and $\tau_{\mathrm{Int}} = 0$ ns[37].

4.1 Calculation of the Normalized Contrast

An asymmetric delay of the grating timing leads to smaller amplitudes of the interference pattern. For large delays the fringes show no spatial modulation. Therefore the calculations consider the momentum distribution $D(p)$ in (41-42). This is done by implementing the beam divergence α, which is related to the Fourier transform $\widetilde{D}(x)$.
For symmetric pulse separation all particle trajectories from the second grating overlap at the third grating and contribute constructively to the interference pattern. Due to the trajectory's different angles of incidence this constructive contribution is restricted to symmetric separation. Deviations from such a symmetric arrangement by a delay of τ lead to an overlap of several relatively shifted interference fringes. This washes out the pattern and reduces the overall contrast. The contrast almost vanishes for an asymmetric pulse separation which yields a continuous fringe shift distribution between 0 and $d/2$. Here d denotes the grating period. This gives an upper bound for the asymmetry of the pulse separation [101]:

$$\tau_{\max} = \frac{d}{2v\tan(\alpha)}. \tag{52}$$

[36] Many experimental imperfections, like deformations of the mirror or limited reflectivity of the mirror, grating laser divergences, limited coherence lengths etc., are difficult to model and therefore not included.

[37] τ_{Ref} corresponds to a slight delay of the last grating pulse separation in the reference mode such that $T_2 - T_1 = T_3 - T_2 - \tau_{\mathrm{Ref}}$. Therefore it makes no difference if the second or third grating timing is delayed. Same holds for τ_{Int} in the interference mode.

The signal S_α caused by a delay of τ, at a grating timing $T = T_2 - T_1 = T_3 - T_2 - \tau$ and a phaseshift of Δx_s, is given by

$$S_\alpha(\Delta x_\mathrm{s}, T, \tau) = S_\mathrm{Avg}(\tau, T) + \Big(S(\Delta x_\mathrm{s}, T, \tau) - S_\mathrm{Avg}(\tau, T)\Big) \times \exp\left[-\left(\frac{\tau}{\tau_\mathrm{max}\sqrt{2\ln(10)}}\right)^2\right], \tag{53}$$

$$S_\mathrm{Avg}(\tau, T) = \frac{1}{N}\sum_{\mathrm{i}=0}^{\mathrm{N}} S(d\frac{i}{N}, T, \tau). \tag{54}$$

For a symmetric pulse separation ($\tau = 0$) S_α is equivalent to the signal S from Equation (45), whereas an asymmetry exceeding τ_max causes averaging of the interference pattern over the whole grating period, represented by S_Avg. A stepwise change of the grating delay τ reveals a Gaussian shape of the reference signal, as shown in 15a.). This accords to the Gaussian shape of the momentum distribution $D(p)$. For a delay of τ_max the signal drops by a factor of 9/10 [83].
The normalized contrast S_N is calculated with $S_\mathrm{N} = (S_\mathrm{Int} - S_\mathrm{Ref})/S_\mathrm{Ref}$, where both values are calculated with S_α. For S_Int the delay is set to $\tau = 0$ and for S_Ref it is set to $\tau > \tau_\mathrm{max}$. Changes of the normalized contrast due to a tilted molecular beam are already included in S_α, because they contribute to S. Also phase shifts due to accelerations a and shifts due to misalignment of the gratings Δx_s are considered.

Reliable evaluation of the normalized contrast requires a sufficient large delay of the grating timing for the reference signal, where the delay has to exclude the possibility of still being in the zone of coherent interference. Due to a tilted molecular beam the measured signal S_α oscillates for grating delays below τ_max [83], shown in Figure 15a.). Detection of the normalized contrast at OTIMA relies on the measurement of S_Ref and S_Int. It is possible to gain different reference values for insufficient asymmetry of the grating timing, represented by the spots in Figure 15a). For a delay of 13 ns (blue) the signal S_Ref is about three times smaller than S_Ref with 27 ns (grey) and about two times smaller than S_Ref for 100 ns (orange). Due to the contribution of S_Ref to the denominator of S_N measurements in the interference mode will gain higher values for $\tau_\mathrm{Ref} = 13$ ns than for $\tau_\mathrm{Ref} = 27$ ns, as shown in Figure 15b). Therefore only pulse separation asymmetries above τ_max deliver a reliable representation of the interference contrast.

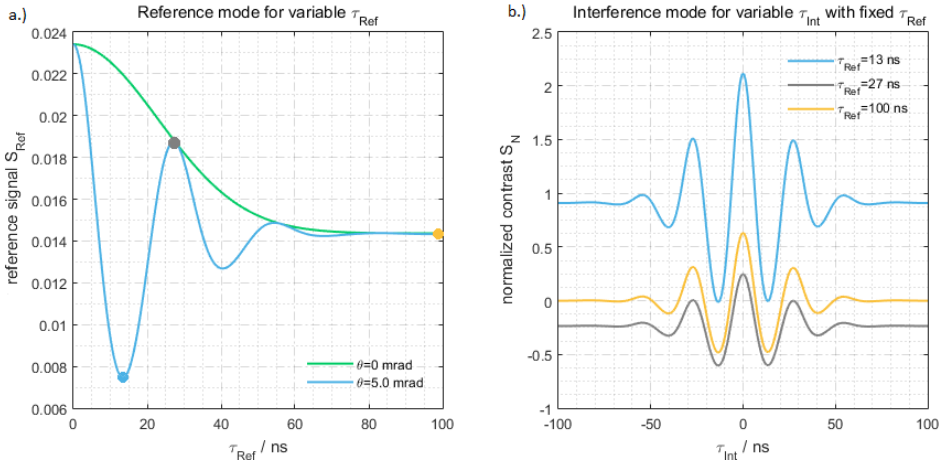

Figure 15: The influence of asymmetry in the pulse separation between $G^{(1)}$-$G^{(2)}$ and $G^{(2)}$-$G^{(3)}$ in the reference mode. a.) shows S_{Ref} for increasing delays τ_{Ref}, revealing oscillations for $\theta \neq 0$ and $\tau_{\mathrm{Ref}} < \tau_{\mathrm{max}}$. b.) shows the normalized contrast S_{N} for a tilt of $\theta = 5$ mrad with fixed grating delays τ_{Ref} in the reference mode (calculation of S_{Ref}) and variable delays τ_{Int} in the interference mode (calculation of S_{Int}). The orange line corresponds to $\tau_{\mathrm{Ref}} > \tau_{\mathrm{max}}$, which is a good measure for the real normalized contrast. For the blue line τ_{Ref} is set to a local minimum of S_{Ref} (blue) which results in an overestimation of the contrast. The grey line represents τ_{Ref} in a local maximum of S_{Ref}. This leads to an underestimation of the normalized contrast.

4.2 The Symmetric Talbot Scan in the Time-Domain

In Chapter 2.4.3 the behavior of the visibility $\mathcal{V}$ is shown for a symmetric variation of the grating pulse separation. Here it is compared to the normalized contrast S_{N}. According to Figure 5a.) both contrast measures have similar maximal values for low average photon absorption numbers $n_0^{(\mathrm{k})}$ which are therefore set to $n_0^{(\mathrm{k})} = 4$. Figure 16a.) shows the modulation of the normalized contrast (solid lines) and the visibility (dotdashed lines) during a symmetric scan of the pulse separation. The two contrast measures show almost the same modulation. Furthermore, the contrast is insensitive to a tilted molecular beam, as shown in Figure 16b.). The figure shows the normalized contrast for fixed $\beta = 0.5$ with and without a tilt of $\theta = 2$ mrad, where both show the same modulation. Even though a deviation of the pulse separation between $G^{(2)}$ and $G^{(3)}$ causes a phase shift of the interference pattern (see Equation (40)), the symmetry of the scan for $G^{(1)}$ and $G^{(2)}$ compensates this shift. This can be seen in Equation (37) by setting $T_1 = T_2$ which yields to $\tau = 0$ in Equation (39) and (40).

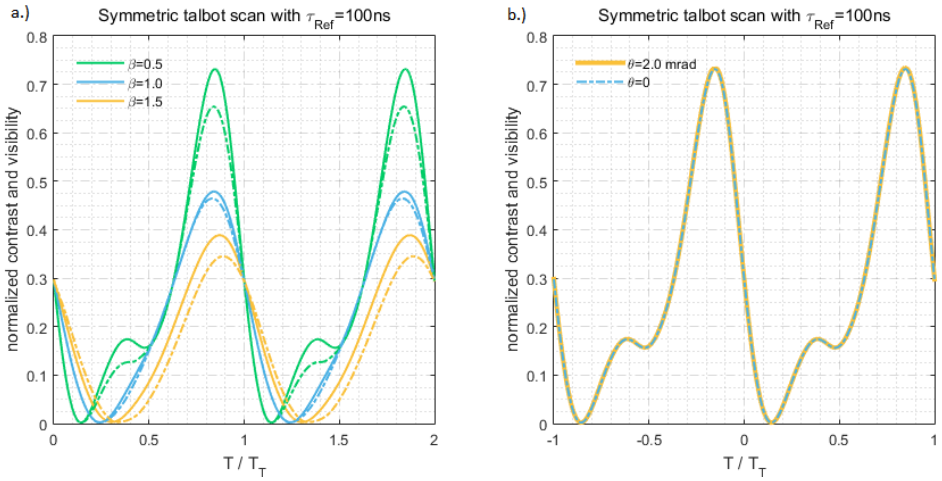

Figure 16: Contrast revivals for a symmetric scan of the grating pulse separation T. a.) The visibility $\mathcal{V}$ (dotdashed lines) and the normalized contrast S_{N} (solid lines) for different particle properties β and $n_0^{(\mathrm{k})} = 4$. Both show almost the same behavior. b.) A tilted molecular beam has no influence on the normalized contrast.

4.3 Dip Measurements

Dip measurements denote an experimental run where one grating pulse separation is changed in the interval $[-\tau_{\max}, \tau_{\max}]$. Chapter 4.1 mentioned the importance of the right amount of grating delay in the reference mode.
In presence of a tilted molecular beam it is therefore better to fix τ_{Ref} and change τ_{Int} instead, as shown in Figure 17a.). The normalized contrast peaks for $\tau_{\mathrm{Int}} = 0$ and decreases symmetrically for both sides ($|\tau_{\mathrm{Int}}| > 0$). Figure 17b.) shows the normalized contrast for varying the grating delay in the reference mode τ_{Ref} and a symmetric grating timing in the interference mode ($\tau_{\mathrm{Int}} = 0$). In absence of any tilts the contrast modulation shows the inverse behavior of a.) with a minimum for $\tau_{\mathrm{Ref}} = \tau_{\mathrm{Int}} = 0$ and maximum for $|\tau_{\mathrm{Ref}}| \geq \tau_{\max}$. Due to this behavior the scan is called dip measurement. For $\theta \neq 0$ the reference signal in the denominator of S_{N} is modulated (see Figure 15) which leads to an overestimation of the normalized contrast. However, within this measurement the wrong approximation can easily be identified by the asymmetric oscillation amplitudes of the contrast.

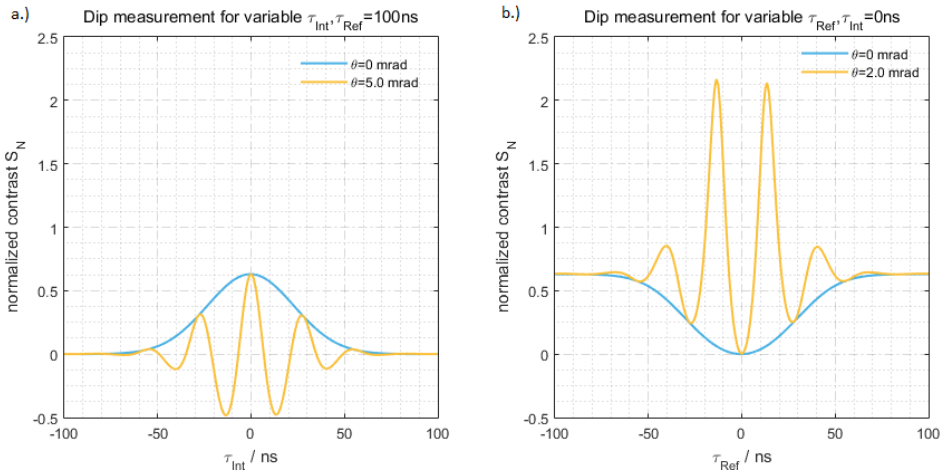

Figure 17: The two possible methods for dip measurements. a.) The reference signal is fixed and the interference signal S_{Int} is varied by changing the grating delay τ_{Int}. This shows a symmetric modulation of the normalized contrast b.) Here the pulse separation asymmetry in the interference mode is fixed while the reference signal S_{Ref} is scanned by changing τ_{Ref}. Only in the absence of tilted beams this offers a reliable representation of the normalized contrast.

The width of the dip[38], and therefore the required grating delays for full mapping, is determined by the beam divergence α. The stronger collimated the beam, the broader is the dip, because of the contribution of α to the denominator of τ_{max} in Equation (52). Figure 18a.) illustrates this behavior for different beam divergences α. For particles with a high optical dipole polarizability (low β values) the peak of Figure 17a.) can even be shifted by a few nanoseconds. Detection of this peak-shift relies on a beam collimation below $\alpha \leq 0.3$ mrad as shown in Figure 18b.). It can be explained by the resonance curves of the Talbot scan. The symmetric Talbot scan from Chapter 4.2 predicts a higher normalized contrast for a timing $T < T_{\mathrm{T}}$. The larger the optical dipole polarizability of the particle, the steeper is the slope. For a negative delay at low β values the increase of S_{Int} may exceed S_{Ref} and yields a shifted maximum of the normalized contrast.

[38] Actually the modulation of the normalized contrast S_{N} looks like a dip only for an asymmetric pulse separation scan in the reference mode. For a scan in the interference mode it looks like a peak.

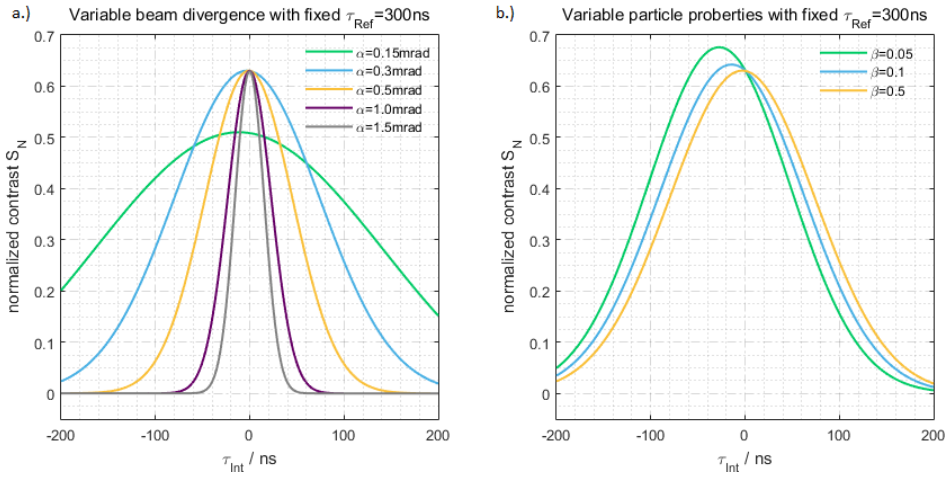

Figure 18: The influence of different a.) beam divergences α and b.) particle properties β on the dip measurement for a grating pulse separation equal to the Talbot time T_T. Different divergences influence the dip-width, whereas variable particle properties show almost no influence on the dip. An exception lies in combinations of small divergences and low β values, where S_N reveals an on β dependent shift of the maximum of S_N.

The influence of β on the peak in Figure 18b.) can almost be neglected, as it is shown for smaller beam divergences in Figure 19a.) where the peak-shift vanishes. This holds for grating delays T equal to the Talbot time T_T. Here the second grating acts as a purely absorptive grating and is therefore independent of the particle properties. Thus variable values of β show the same behavior. This changes for grating delays slightly detuned from the Talbot time. Figure 19b.) shows a symmetric change of the pulse separation T by $\pm 0.01\ T_\mathrm{T}$. Here the phase modulation of the second grating also contributes to the interference pattern.
In case of a tilted molecular beam the dip measurement reveals oscillations between positive and negative values of S_N. The larger the tilt the shorter is the period. Such kind of measurements are used to scan the spatial interference pattern, as represented in Figure 20. Knowledge of the beam tilt θ allows straight forward extraction of the grating period and works for sufficiently collimated beams, as Figure 20b.) shows. For a fixed tilt of $\theta = 2$ mrad beam divergences below $\alpha = 1$ mrad are required to resolve at least one negative side wing of the modulated dip.

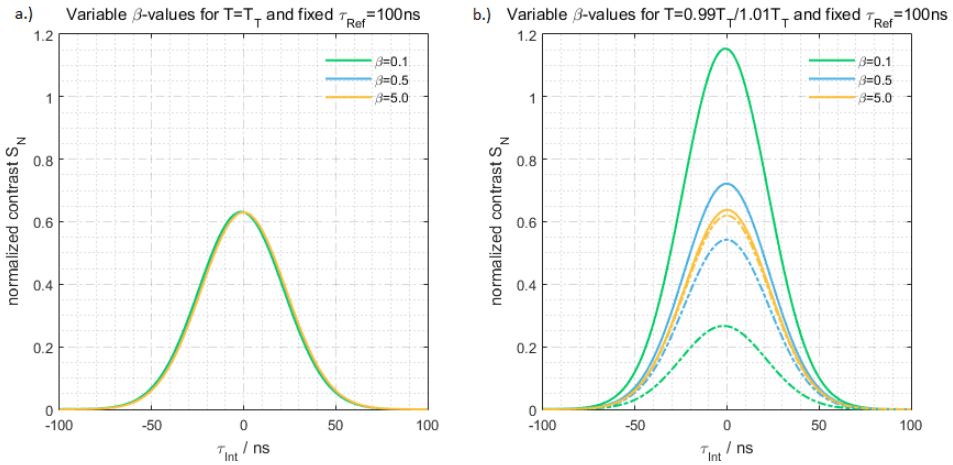

Figure 19: The influence of different β values on the normalized contrast. a.) For symmetric grating delays T_T and a fixed $\tau_\mathrm{Ref} > \tau_\mathrm{max}$ variable β values have no influence on the contrast, since $G^{(2)}$ acts as purely absorptive grating. b.) For slight deviations of the Talbot time β has an influence on the normalized contrast due to the phase contribution of the second grating. The solid lines represent symmetric pulse separations by $-0.01\ T_\mathrm{T}$ while the dotted lines correspond to $+0.01\ T_\mathrm{T}$.

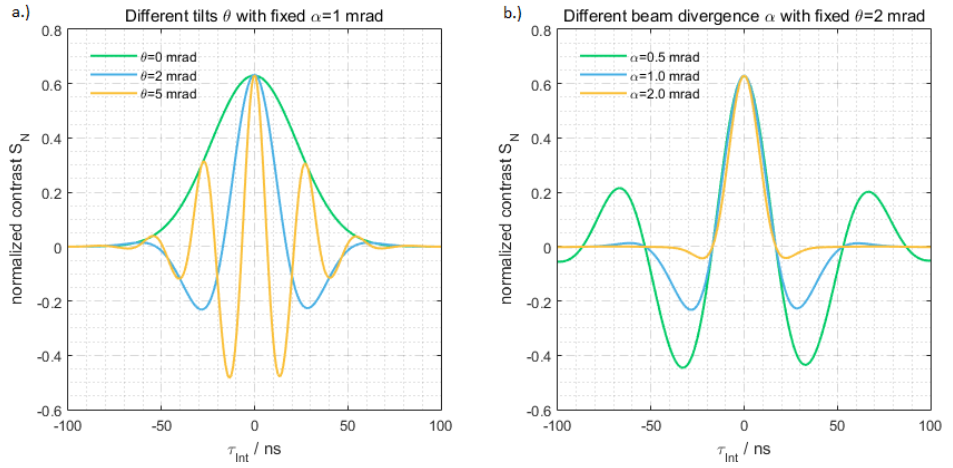

Figure 20: The influence of a tilted molecular beam onto the Dip-measurement. a.) shows oscillations within the dip for several tilts θ. The oscillation period shrinks with increasing tilts. b.) Variable beam divergences α for a fixed tilt of $\theta = 2$ mrad show that only sufficient collimated beams allow detection of such oscillations.

5 Results

The biggest challenge in all measurements with Gramicidin is the preparation of a stable molecular beam with constant particle countrates during the whole measurement. Various adaptions to the source conditions, as described in Section 3.1.2, are required to allow measurements over several hours. Nevertheless the beam conditions were sufficient to enable interference measurements with Gramicidin. Therefore this chapter presents the first results of biopolymer interference.
Furthermore, employing a femto-second laser proved crucial in terms of signal intensity and stability. This even allowed desorption and detection of a monodisperse beam consisting of intact tailor-made proteins with masses up to 20 000 amu.

5.1 Femtosecond Desorption of Proteins

The typical interference measurement at OTIMA for a single point of a 1D-Talbot-carpet takes about $5-10$ minutes. Without knowledge of the particle properties and full characterization of the experimental setup a single point is not sufficient to claim the quantum nature of the interference contrast. Instead, dip measurements are performed as described in Chapter 4.3. Such measurements require several data points and therefore at least two hours of stable signal.
The time dependence of the particle count rates is shown in Figure 21, where an exponential decay ($y = a \times \exp(-x/b)$) is fitted to the data points. For all three measurements the laser beam was focused onto the carbon wheel with a diameter of about 100 μm. The pulse energy was kept below 1 mJ for the ns-laser and 20 μJ for the fs-laser. Without re-coating of the felt wheel (blue line) and using the ns-laser the signal drops to 20 % of the initial value within 30 minutes. Even for continuous coating of the wheel (orange line) the signal shows a decay to 50 % within one hour. A major problem is the coating of the focusing optics and the source chamber during operation. A collision cell and a rotating glass slide protected the source from coating. Still, the valve contamination made the measurments more complicated. However, the usage of a fs-laser (green line) significantly improved the long-time stability of the source which made the sample slide unnecessary. Even after one hour the signal had only decayed by 10%. The fs-pulses dramatically reduced the surface coating is.

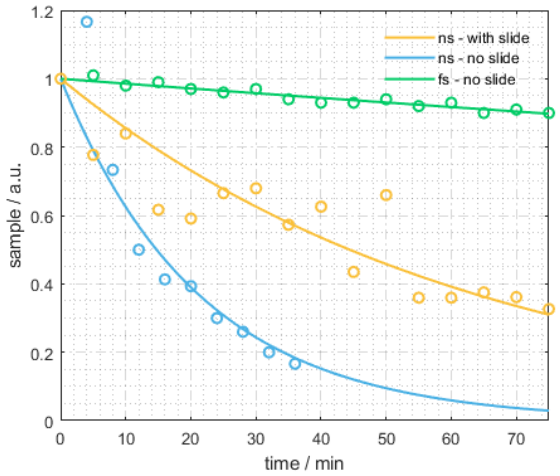

Figure 21: The signal decay of Gramicidin during a measurement. The green line corresponds to the fs-laser desorption, whereas the orange and the blue graph show the signal decrease for the ns case with (orange) and without (blue) the sample slide. All lines show an exponential decay of the signal intensity, which is probably caused by coating of the optics. This basically reduces the desorption laser pulse energy deposited on the surface of the carbon wheel. The data points were normalized to the initial value and therefore overlap at the first point (t=0).

Figure 22 shows the velocity distribution of Gramicidin injected into the supersonic beam of argon using fs-laser desorption. The velocity distribution was detected by scanning the post ionization laser over the molecular beam[39]. Based on the calculations of Equation (46) the maximal flow velocity of argon with an initial temperature of 300 K is in the range of 560 m/s. A fit of Equation (9) to the data reveals good agreement between theoretical and experimental values with $v_{\mathrm{avg}} = (587 \pm 1)$ m/s. Extraction of the translational temperature provides information about the cooling process during expansion. Measurements revealed $T_{\mathrm{trans}} = (210 \pm 2)$ K for Gramicidin $A1$, which is about 90 K below the initial temperature of the sample. Presumably, the rotational and vibrational temperatures are higher. Nevertheless, the measurement shows that the source conditions are sufficient to accelerate the orthogonally injected, about 50 times more massive molecules towards the maximum velocity of the carrier gas itself.

[39]This is only a good measure under the assumption of a Dirac pulse of the valve.

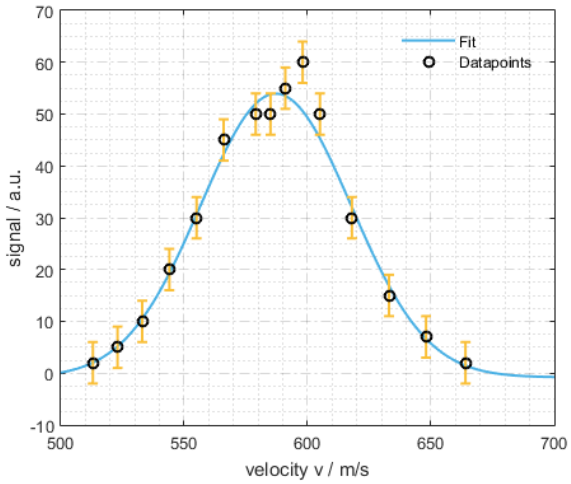

Figure 22: The velocity distribution of a molecular beam of Gramicidin at OTIMA detected with the ToF-MS. At valve opening widths $\Delta t_v \approx 20$ μs and a carrier gas pressure of $p \approx 24$ bar the beam revealed an average flow velocity of ≈ 590 $\frac{\mathrm{m}}{\mathrm{s}}$. A fit according to Equation (9) is in good agreement with predictions of super sonic beam theory.

Another benefit of the fs-laser is an increase of the signal intensity. In Chapter 3.1.4 it was predicted that an increase in the laser intensity leads to more efficient desorption of single molecules and therefore attenuation of phase explosions and spallation. The strongly reduced coating of the source chamber combined with the increasing signal intensities favor fs desorption.
An increase in signal intensity is shown in Figure 23. It compares the time-of-flight mass spectra of desorbed artificial proteins with a mass of 12 314 amu for fs- and ns-pulses[40]. For both cases the mass spectra show several fragments but no intact protein itself. Fragmentation is probably caused during the ionization process. The dominant peaks in both spectra with $m = 11\,770$ amu differ by a factor of two in intensity, revealing an enhancement of isolated molecules when using fs-pulses even though the pulse energy is 100 times smaller than for the ns-laser beam. The spectrum also reveals fragments in almost equal distances of $780 - 790$ amu. The fragments probably correspond to breaks in the main chain of the 12 312 amu particle.

[40]The spectrum is calibrated with a 20 196 amu protein. Since the mass deviation of the fragments is almost similar to the chain-subgroups of Figure 24, the approximation is assumed to be correct.

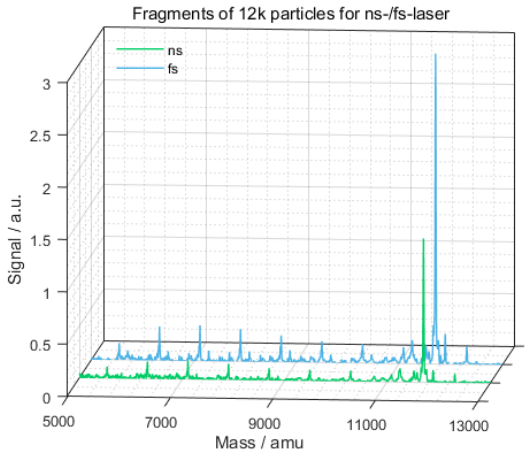

Figure 23: Laser desorption VUV-postionization mass spectra of tailor-made proteins with a nominal mass of 12 314 amu for ns- (green) and fs-pulses (blue). In both cases the mass spectra show several fragments with comparable relative intensity distribution. The intensity of the strongest peak at 11 770 amu differs by a factor of almost two, indicating an increase in desorption efficiency for a fs-pulse. The fragments deviate by a mass of $780 - 790$ amu, which agrees with the mass of the subgroup depict in Figure 24. This strengthens to the assumption of a break in the main chain.

Figure 24 shows the structure of the particles with the fluorinated side-chains. They were attached to enhance single photon ionization and allow efficient detection in the ToF-MS.

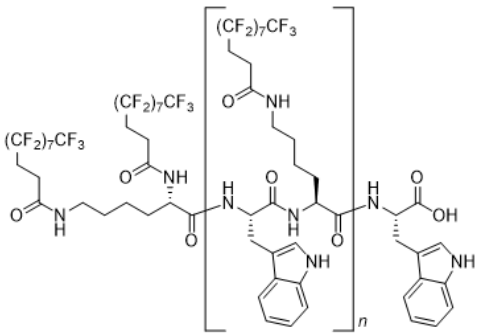

Figure 24: The structure of the tailor-made protein with a mass of 12 312 amu. The perfluorinated ligands of the molecule allow enhanced ionization due to single photon absorption. The molecule consists of $n = 14$ repetitive groups, each with a mass of $m = 788$ amu.

The repetitive subgroup in the squared brackets has a mass of $m = 788$ amu which is in good agreement with the fragment distances. The spectrum also shows very low countrates for intact particles. Therefore almost all particles fragment either during the desorption-process or during post ionization.
Using fs-pulses transports more heat to the molecules and forces them to undergo faster transition from solid state to gas phase [88]. This imposes the possibility of a higher fraction of broken molecules due to insufficient cooling after desorption. Missing cooling can be negated by observation of the fragmentation distribution of both mass spectra, as it is done in Figure 25. All spectra show the same distribution for fs- and ns-pulses but different amplitudes as it is denoted by the different y-labels of the plot. Still, this does not allow to decide if fragments are produced in the source during desorption or by photofragmentation during the post-ionization process. However, it indicates equivalent cooling and fragmentation for fs- and ns-injected molecules.
Even further improvement of Gramicidin desorption is possible by increasing the pulse-lengths of the desorption laser from 300 fs to 10 ps. The signal intensity increases by a factor of two when the pulse length is increased to 10 ps, as shown in Figure 26, with a constant pulse energy of 20 μJ and a laser spot diameter of 100 μm. Gramicidin was desorbed using the fundamental wavelength of the laser ($\lambda_L = 1030$ nm) to prevent changes of the laser pulse length due to the harmonic generator. Since the signal intensities for Gramicidin were almost equal for $\lambda_L = 1030$ nm and $\lambda_L = 343$ nm the same enhancement can be assumed for the latter. The data points are averaged over 10 s measurement with a repetition rate of 100 Hz. This duration was

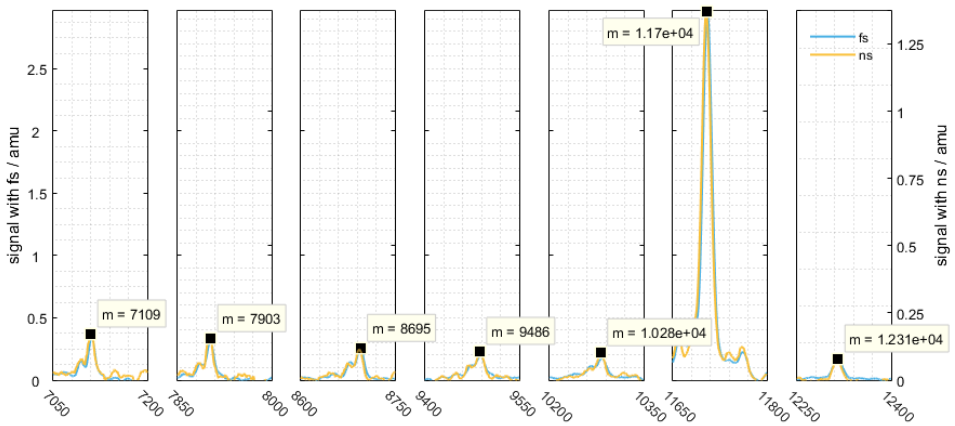

Figure 25: The fragment distribution of the desorbed 12 312 amu particles for 4 ns and 300 fs puls lengths. All of the peaks show the same allocation for ns- and fs-pulses, but differ by a factor of almost two.

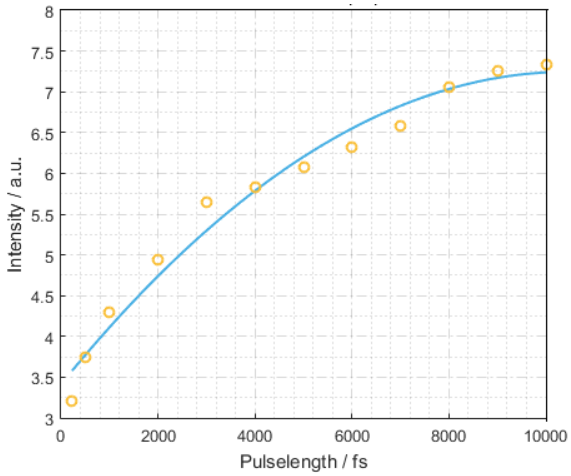

Figure 26: The signal intensity of Gramicidin increases with the laser pulse length. The transition from 300 fs to 10 ps at a constant pulse energy of 20 μJ doubled the countrate but also doubled the sample consume. The laser beam was focused to 100 μm at a wavelength of $\lambda_{\mathrm{L}} = 1030$ nm.

sufficient to see a decrease in intensity of 30 % for pulse lengths of 10 ps. Overall the fs-laser desorption with supersonic expansion looks promising for future experiments with biomolecules of higher mass and complexity. As a first demonstration of its potential Figure 27 reveals the creation of an almost monodisperse molecular beam of isolated and neutral 20 196 amu particles. They are tailor-made, consist of 50 functionalized amino acid residues and their structure is equivalent to the Figure 24 with $n = 24$ subgroups. For simpler calibration of the ToF-MS the 12 312 amu particles from previous measurements were added to the sample.

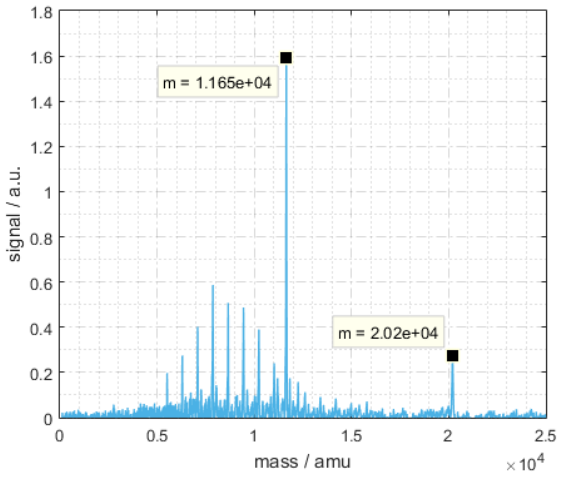

Figure 27: Detection of an artificial protein with the mass of 20 196 amu. The structure of the molecule is shown in Figure 24 for $n = 24$ subgroups. For simpler mass- and ToF-calibration the 12k-particles were added to the sample. The fragments deviate by a mass of $780 - 790$ amu, which agrees with the mass of the subgroup. This leads to the assumption of a break in the main chain. The depict mass spectrum is baseline corrected, where the baseline is laid through the minima of the raw mass-spectrum, as it is shown in the appendix.

5.2 Interference Measurements with Gramicidin

Even though the combination of fs-laser pulses with the biomolecular source apparently is the key to interference measurements with Gramicidin the following results are based on signals obtained with the ns-laser.

Figure 28 shows the modulated mass spectrum of Gramicidin for a single peak interference measurement. In the reference mode (orange), where the last grating was detuned by $\tau_{\mathrm{Ref}} = 200$ ns, the mass spectrum of Gramicidin shows lower intensities than in the interference mode (blue), where $\tau_{\mathrm{Int}} = 0$ ns. This is consistent with expectations, since the spatial molecular density-distribution reveals barely no modulation in the reference mode, resulting in higher beam depletion than it is the case for the interference mode where the density-distribution is more located in the nodes $G^{(3)}$. For comparison, Figure 28a.) displays the mass spectrum of TPP which shows no difference between the two modes. Since TPP ($m = 512$ amu) is almost three times lighter than Gramicidin ($m = 1882$ amu) it should also reveal interference in the third Talbot order. During the interference measurements TPP revealed very high transmission-rates of ≈ 60 %. Section 3 mentioned good contrast for transmission rates between 20 %−30 %. For a higher trans-

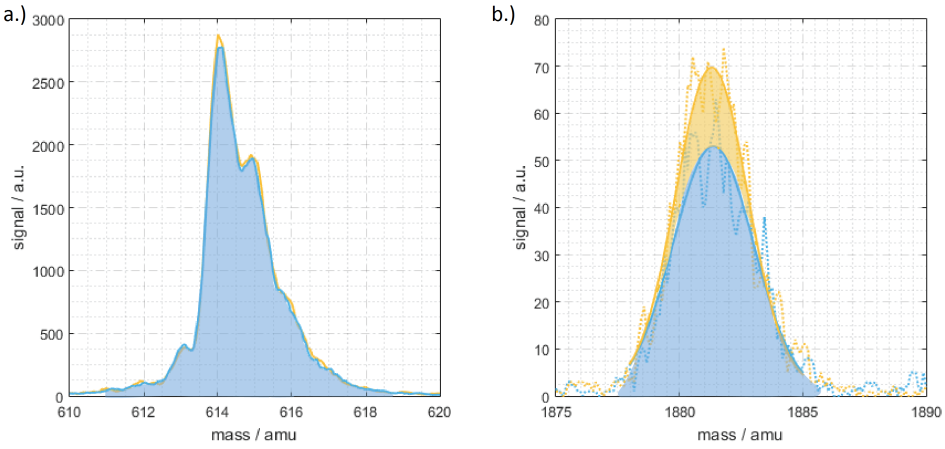

Figure 28: The single point interference measurement with $\tau_{\mathrm{Ref}} = 200$ ns and $\tau_{\mathrm{Int}} = 0$ ns in a.) shows almost no difference between the interference mode (blue) and reference mode (orange) for Tetraphenylporphyrin (TPP). This is the result of grating transmission rates of 60 %, which restricts the contrast to values below 5 %. b.) reveals a normalized contrast of $S_{\mathrm{N}} = 25$ % for Gramicidin.

mission rate[41] of all three gratings Figure 10 predicts contrast values below 5%. Therefore the contrast of TPP vanishes. Since OTIMA interference of TPP was already seen before [83] this probably indicates rough alignment of the optical gratings and a higher absorption cross section of Gramicidin compared to TPP. The single point measurement revealed a normalized contrast of

$$S_N = 0.25 \pm 0.08 \tag{55}$$

Figure 29a.) shows how the contrast changes when the last grating is delayed by τ_{Ref} in a range of $\pm$ 100 ns, in steps of 20 ns. The molecular beam was collimated to a square of [0.4 mm $\times$ 0.4 mm] with a beam divergence of $\alpha \leq 0.4$ mrad. Each point represents 5000 averaged mass spectra. Even though the error-bars exceed the contrast values there is still a perceiveable modulation. As mentioned in Section 3.4 the error bars predict a worst case scenario with a maximum of one detected particle per frame and also may therefore be seen as an upper bound of the error. The measurement reveals an asymmetric modulation around the y-axis. This is explained by an overall grating phase shift Δx_{s}, which is probably caused by the mirror roughness as mentioned in Chapter 3.3. Therefore a fit $y = a \times \exp\left(-(x/b)^2\right) \times \sin(cx + d) + e$ is applied to the data points and reveals $|a| = 0.14$. This represents the maximal normalized contrast S_{N}. The fit also yields an overall grating shift of 41 nm, which is more than half of the grating period. The shift is probably caused by the mirror roughness. Figure 29b.) shows that the fitted signal can be interpreted with the help of the simulations mentioned before. The variable parameters are the beam divergence α, the beam tilt θ, the average number of absorbed photons n_0 and β which is proportional to the absorption cross section and optical polarizability. The latter shows the weakest influence on the outcome of the measurements, since the interference mode sets the grating timing to the Talbot time, where $G^{(2)}$ acts as pure absorbtive grating. Consistency between the fit and the simulation is obtained for $\alpha = 0.4$ mrad, $\theta = 1.8$ mrad and $n_0 = 2.9$. The tilt angle was independently measured with an alignment laser, reflected by a mirror mounted on the source and revealed $\theta \approx$ 2 mrad, in good agreement with the simulations and fit. Also the photon absorption number of $n_0 = 2.9$ seems reasonable compared to earlier measurements with Anthracene [99]. Section 4.3 explains the overestimation of the contrast for a detuning of τ_{Ref} in presence of a tilted molecular beam, which is also the case for the depict measurement. Therefore the calculation with adapted parameters is used to predict the signal modulation in case of detuning τ_{Int} with fixed $\tau_{\mathrm{Ref}} = 200$ ns as shown in Figure 30. The simulation reveals a lower maximum contrast of $S_{\mathrm{N}} = 0.13$.

[41] That is also the reason for the higher signal intensity of TPP in Figure 28. About 0.8^3 of the initial TPP particles escape from the TLI, whereas only 0.22^3 of the Gramicidin particles are detected afterwards.

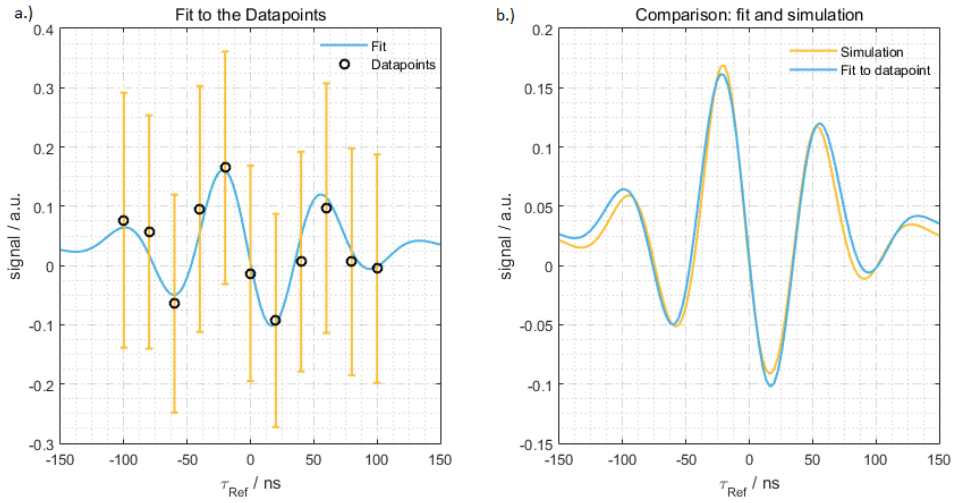

Figure 29: Interference dip measurement of Gramicidin with detuning in the reference mode. a.) The data points reveal a sinusoidal modulation due to the tilted molecular beam, with a maximum contrast of $S_N = 0.14$. b.) The fit to the data points in a.) is used to find the correct parameters for the simulation. For $\alpha = 0.4$ mrad, $\theta = 1.8$ mrad and $n_0 = 2.9$ the simulation is able to reproduce the detected modulation of the interference measurements with Gramicidin.

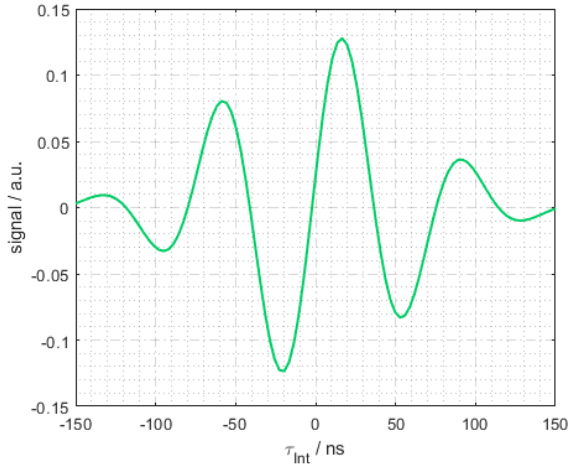

Figure 30: Simulation of the modulated dip in case of detuning τ_{Int} instead of τ_{Ref}. The parameters for the simulation were adapted to reproduce the measurements from Figure 29. The simulation reveals a lower maximum contrast of $S_N = 0.13$.

6 Conclusions and Outlook

The first interference measurements with Gramicidin revealed a single point contrast of $S_N = 25\%$, which is comparable to previous interference measurements at OTIMA [83]. The dip measurement revealed a maximal contrast of $S_N = 14$ %. This is not very high and the error bars are larger than the contrast modulation, but still the consistency between simulations and the data as well as the detection of the spatial fringe patterns and the consistency with the manually measured molecular beam tilt might be evidence for genuine interference. Therefore, this thesis presents the first interference measurements of a large biopolymer.
The implementation of the molecular beam divergence and tilt to the theoretical models allows the consistent prediction of experimental results with the measurement modes actually used at OTIMA. This further improved the characterization of the experiment itself, alike the optimization of the detection parameters. Chapter 4.3 mentioned the importance of laser detuning in the interference mode instead of the reference mode. This circumvents contrast overestimation for tilted molecular beams, which may cause an offset of the detected dip. An appearance that has been unclear previously when comparing the experimental data to theoretical models at hand.
Several adaptions to the molecular source were applied to improve the signal stability during measurements. The key change to the setup was undoubtedly the combination of fs pulses with a tight focus on the carbon wheel. The flux threshold for increased desorption of 10^{13} W/cm^2, mentioned in several articles, can clearly be verified. Comparison of the mass spectra acquired with nanosecond or femtosecond desorption showed similar fragmentation patterns for both pulse lengths, which indicates comparable internal temperatures of the detected molecules.
For future interference measurements especially for interference-assisted spectroscopy [27] it will be necessary to improve the molecular beam. The attachment of a fs-laser will definitely help to improve the long-time stability of the source, but also the coating mechanism needs improvement. Currently a sample slide contains the molecular sample and delivers the molecular powder to the felt wheel, which further coats the carbon wheel. This works out fine for molecules available in sufficient amounts. For tailor-made or expensive molecules this inefficient loading mechanism is prohibitive. Therefore a liquid supply mechanism is currently under construction and will be tested soon. It is based on a coating from a solution of the molecules and a solvent with sufficiently low vapor pressure.
Another modification that could be implemented to the next source setup of OTIMA is a tiltable molecular beam. The measurements revealed simpler detection of the interference spatial densitiy distribution for tilted beams. Fine adjustment and observation of the tilt will simplify ongoing measurements. For interference-assisted spectroscopy the dip modulation may also

improve the sensitivity of the measurement since it allows to increase the normalized contrast by setting τ_{Ref} to a minimum of S_{Ref}, as mentioned in Chapter 4.3. Even though this increase of the contrast is a consequence of the detection mechanism and not real quantum behavior it still reveals high sensitivity to small shifts of the molecular beam, which is the key element of interference-assisted spectroscopy.
Since progress in molecule interferometry further exceeds in terms of mass the question arises if it could be possible to interfere living organisms, like small viruses with masses in the range of $10^6 - 10^7$ amu. They have proven to survive low-vaccum conditions [102] and behave like dielectric spheres [103]. Therefore they seem to be the optimal candidates to push interference measurements to the next level: Living organisms delocalized in space. The presented interference measurements are therefore pointing the way ahead, in terms of probing source and experimental requirements.

7 Acknowledgements

The years of my studies were full of beautiful moments, great experiences, hard challenges and personal achievements. Through all this time there were a bunch of people supporting, inspiring and motivating me to continue and never give up. Therefore I want to devote this chapter to some of them, knowing that it's not possible to mention everyone. After one and a half years in an experimental group it actually feels like saying goodbye to good old friends - so please excuse me for being a little bit sentimental.
Unquestionably I want to thank Markus Arndt for the opportunity to be a part of his group . Thank you for your support, your trust in me and for letting me work on one of your experiments. I would also like to thank Armin Shayeghi for being my colleague, mentor and most of all for becoming a good friend. It was your stamina and your intention to never give up that impressed me and guided me through any experimental difficulties. A simple thank you is probably not enough to honor all the support you offered me within the last year, but maybe this is: Thank you to the god of alignment! I also want to thank the MQ3-gang for all the entertaining hours in the laboratory. You were always able to make me feel better when the experimental results wanted to make me cry. To our finance and administration ladies: Thank you for the funny discussions in the morning, the friendly ear and the both-sided chocolate delivery.
Within my first weeks at university I met Claudia, Julia and Tobias and I'm very happy to still count them to my closest friends. Solving equations, laughing, eating, doing sports - all of it makes more fun when you are around. Later on I met the other 'Nerds': Annie, Florian, Martin, Simon and Thomas. Young and amazing physicists, who also share my affection for riddles and other challenging adventures. Thank you for many unforgettable moments.
Undeniably I also have to thank my girlfriend Steffi for all the support within my last years of study. Thank you for your trust in me, your encouraging and motivating words and the wonderful years together. And after all I really want to thank my family for the support within the last 27 years.
Realizing that it was your emotional backing, your help and of course your believes that gave me the strength to succeed in my studies, I have to mention one more time how happy it makes me to have parents, sisters, brothers-in-law and a girlfriend like you! And things like this confirm me everyday:

"Yes, we invest in gold bars too! We have four of them and they're called Sonja, Doris, Petra and Georg."
- Anna Richter

8 Appendix

8.1 Biomolecules

Biomolecules are carbohydrates that are found in living organisms, often containing nitrogen, oxygen, phosphorus, and sulfur atoms. In a simple picture they can be divided into two groups: monomers and biopolymeres. Lipids, vitamins, amino acids, nucleotides and monosaccharides are complex monomers with a mass typically below 1000 amu. DNA and proteins are biopolymeres, chains composed of a series of common building blocks [104].

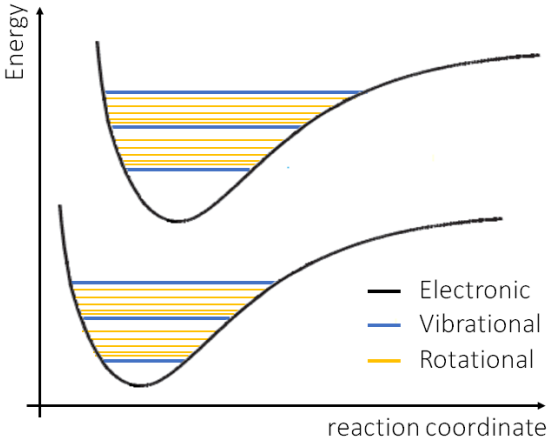

Figure 31: A sketch of the electronic states of diatomic molecules. Each electronic state has a vibrational fine structure, where each vibrational level further has a rotational fine structre. Similar diagrams can be drawn for all $3N-6$ normal modes of the N-atomic molecules

Due to their complex molecular geometries with many internal degrees of freedom, biomolecules offer very complex energy landscapes. Such hyper-surfaces enable diverse excited state dynamics [105] which are much harder to predict than it is the case for isolated atoms. Each molecular electronic state has an underlying vibrational level structure, each with a rotational fine structure. However, since the distance between two rotational states scales inversely proportional to the moment of inertia, the rotational level structure of large molecules is often not resolveable in an experiment. Figure 31 sketches two electronic states of a diatomic molecule, which corresponds to the $3N-6$ dimensional projection of the energy landscape of a N-atomic molecule along the most favorable energetic path through a minimum, the so-called reaction coordinate.

8.2 Baseline Correction

The depict mass spectra of the 20 196 amu and 12 314 amu particles in Chapter 5.1 are provided with a baseline correction. The baseline was drawn manually such that it includes all local minima of the spectrum. Since it still includes all the sub-peaks of the spectra it does not sophisticate the measurement. In Figure 32 one can see the smoothed data after applying a running average with 100 samples to the raw data. The red line in the plot corresponds to the drawn baseline. The baseline-corrected signal is shown in Figure 27.

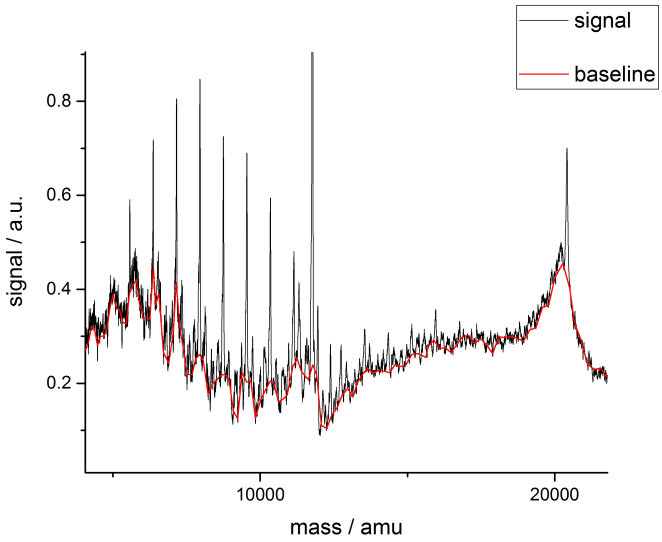

Figure 32: The baseline correction of the 20 196 amu and 12 314 amu particle measruements. The black line corresponds to a running average with 100 samples, whereas the red line shows the applied baseline.

References

[1] Albert Kuemmel-Schnur and Jens Schröder. *Aether : ein Medium der Moderne*. Bielefeld : Transcript, 2008.

[2] V. B. Meyer-Rochow and J. Gal. A "Polar Biology Publication" that prevailed: forces at work when Penguins Poo. *Polar Biol.*, 29(7):541–542, 2006.

[3] M. Planck. On an Improvement of Wien's Equation for the Spectrum. *Verh. Deut. Phys. Ges*, 2:202–204, 1900.

[4] Albert Einstein. Über einen die Erzeugung und Verwandlung des Lichtes betreffenden heuristischen Gesichtspunkt. *Ann. Phys.*, 322(6):132–129, 1905.

[5] Ernst Schrödinger. Quantisierung als Eigenwertproblem. *Ann. Phys.*, 385(13):437–490, 1926.

[6] Thomas Young. Experimental Demonstration of the General Law of the Interference of Light. *Philos. Trans. R. Soc. London*, 94, 1804.

[7] Louis de Broglie. Waves and Quanta. *Nature*, 112(2815):540, 1923.

[8] L. Marton. Electron Interferometry. *Science (80-.).*, 118(3069):470–474, 1953.

[9] Helmut Rauch. Neutron Interferometry. *Science (80-.).*, 262(5138):1384–1385, 1993.

[10] Alexander D. Cronin, Jörg Schmiedmayer, and David E. Pritchard. Optics and interferometry with atoms and molecules. *Rev. Mod. Phys.*, 81(3):1051–1129, 2009.

[11] C. J. Bordeé. Atomic interferometry with internal state labelling. *Phys. Lett. A*, 140(1-2):10–12, 1989.

[12] Michael S. Chapman, Troy D. Hammond, Alan Lenef, Jorg Schmiedmayer, Edward Smith, David E. Pritchard, and Richard A. Rubenstein. Photon Scattering from Atoms in an Atom Interferometer: Coherence Lost and Regained. *Phys. Rev. Lett.*, 75(21):3783–3787, 1995.

[13] W. Schöllkopf and J. P. Toennies. Nondestructive mass selection of small van der waals clusters. *Science*, 266(5189):1345–8, 1994.

[14] Olaf Nairz, Björn Brezger, Markus Arndt, and Anton Zeilinger. Diffraction of Complex Molecules by Structures Made of Light. *Phys. Rev. Lett.*, 87(16):160401, 2001.

[15] Markus Arndt, Thomas Juffmann, and Vlatko Vedral. Quantum physics meets biology. *HFSP J.*, 3(6):386–400, 2009.

[16] Wojciech H. Zurek. Decoherence and the transition from quantum to classical. *Phys. Today*, 44(10):36–44, 1991.

[17] Lucia Hackermüller, Klaus Hornberger, Zeilinger Anton Brezger Björn, Markus Arndt, Björn Brezger, Anton Zeilinger, and Markus Arndt. Decoherence of matter waves by thermal emission of radiation. *Nature*, 427(February):711–714, 2004.

[18] Magdalena Zych, Fabio Costa, Igor Pikovski, and Caslav Brukner. Quantum interferometric visibility as a witness of general relativistic proper time. *Nat. Commun.*, 2(1), 2011.

[19] Serge Reynaud, Brahim Lamine, Astrid Lambrecht, Paulo Maia Neto, and Marc Thierry Jaekel. Hyper and gravitational decoherence. *Gen. Relativ. Gravit.*, 36(10):2271–2288, 2004.

[20] Jess C. Riedel. Direct detection of classically undetectable dark matter through quantum decoherence. *Phys. Rev. D*, 88(11):116005, 2013.

[21] Lajos Diosi. Models for universal reduction of macroscopic quantum fluctuations. *Phys. Rev. A*, 40(3):1165–1174, 1989.

[22] Roger Penrose. On Gravity's role in Quantum State Reduction. *Gen. Relativ. Gravit.*, 28(5):581–600, 1996.

[23] William Marshall, Christoph Simon, Roger Penrose, and Dik Bouwmeester. Towards Quantum Superpositions of a Mirror. *Phys. Rev. Lett.*, 91(13):130401, sep 2003.

[24] Markus Arndt and Klaus Hornberger. Testing the limits of quantum mechanical superpositions. *Nat. Phys.*, 10(4):271–277, 2014.

[25] Sandra Eibenberger, Stefan Gerlich, Markus Arndt, Marcel Mayor, and Jens Tüxen. Matter-wave interference of particles selected from a molecular library with masses exceeding 10 000 amu. *Phys. Chem. Chem. Phys.*, 15(35):14696, 2013.

[26] Markus Arndt. De Broglie's meter stick: Making measurements with matter waves. *Phys. Today*, 67(5):30–36, 2014.

[27] Jonas Rodewald, Philipp Haslinger, Nadine Dörre, Benjamin A. Stickler, Armin Shayeghi, Klaus Hornberger, and Markus Arndt. New avenues for matter-wave-enhanced spectroscopy. *Appl. Phys. B Lasers Opt.*, 123(1):1–8, 2017.

[28] William R. Oegerle and John R. Sabin. On the CNDO determination of the molecular conformation and properties of Glycine and its zwitterion. *J. Mol. Struct.*, 15:131–136, 1973.

[29] A. Kantrowitz, J. Grey, Precollimation Gain, and I. N. Intensity. A high intensity source for the molecular beam. Part I. Theoretical. *Rev. Sci. Instrum.*, 22(5):328, 1951.

[30] D. Miller. *Atomic and Molecular Beam Methods, Vol. I.* Oxford University Press, 1988.

[31] Raymond Serway. *Physics for Scientists and Engineers with Modern Physics.* Saunders College Publishing, 3rd edition, 1990.

[32] Michael D. Morse. *Atomic, Molecular, and Optical Physics: Atoms and Molecules.* Experimental Methods in the Physical Sciences, volume 29, edition, 1996.

[33] Allan Pierce. *Acoustics: An Introduction to Its Physical Principles and Applications*, volume 34. 1989.

[34] J. B. Anderson and J. B. Fenn. Velocity Distributions in Molecular Beams from Nozzle Sources. *Phys. Fluids*, 8(5):780, 1965.

[35] J. Ashkenas and F. Sherman. *Rarefied Gas Dynamics, 4th Symposium, Vol. II.* Academic Press, New York, 1966.

[36] G. M. McClelland, K. L. Saenger, J. J. Valentini, and D. R. Herschbach. Vibrational and rotational relaxation of iodine in seeded supersonic beams. *J. Phys. Chem.*, 83(8):947–959, 1979.

[37] Robert L. Deleon and J. S. Muenter. Vibrational relaxation of linear molecules in a nozzle expansion. *Chem. Phys. Lett.*, 111(1-2):147–150, 1984.

[38] Philip C. Palma, Paul M. Danehy, and A. F. P. Houwing. Fluorescence Imaging of Rotational and Vibrational Temperature in Shock-Tunnel Nozzle Flow Introduction. *AIAA J.*, 41(9):1722–1732, 2003.

[39] H. Zacharias, M. M.T. Loy, P. A. Roland, and A. S. Sudbo. Rotational and electronic relaxation in pulsed supersonic beams of NO seeded in He and Ar. *J. Chem. Phys.*, 81(7):3148–3157, 1984.

[40] O. Hagena and W. Henkes. Untersuchung der thermischen relaxation bei düsenströmungen durch analyse der gaskinetischen geschwindigkeitsverteilung. *Zeitschrift fur Naturforsch. - Sect. A J. Phys. Sci.*, 15(10):851–858, 1960.

[41] Bernard B. Hamel. Kinetic Theory of Source Flow Expansion with Application to the Free Jet. *Phys. Fluids*, 9(5):829, 1966.

[42] Alexander Nass and Erhard Steffens. Direct Simulation of Low-Pressure Supersonic Gas Expansions and its Experimental Verification. *Nucl. Inst. Methods Phys. Res.*, 598(3):653–666, 2009.

[43] Ugur Sezer, Philipp Geyer, Moritz Kriegleder, Maxime Debiossac, Armin Shayeghi, Markus Arndt, Lukas Felix, and Marcel Mayor. Selective photodissociation of tailored molecular tags as a tool for quantum optics. *Beilstein J. Nanotechnol.*, 8(1):325–333, 2017.

[44] G. Meijer, M. S. de Vries, H. E. Hunziker, and H. R. Wendt. Laser Desorption Jet-Cooling of Organic Molecules. *Appl. Phys. B*, 51(6):395–403, 1990.

[45] P. Raghuraman and P. Davidovits. Velocity slip of gas mixtures in free jet expansions. *Phys. Fluids*, 21(9):1485, 1978.

[46] Bermann and Schäfer. *Lehrbuch der Experimentalphysik Band 3 - Optik.* Walter de Gruyter, 2004.

[47] Paul A. Tipler and Gene Mosca. *Physik für Wissenschaftler und Ingenieure.* Spektrum Akademischer Verlag, 2009.

[48] Max Born and Emil Wolf. *Principles of Optics.* Cambridge University Press, 1999.

[49] Alain Miffre, R. Delhuille, B. Viaris De Lesegno, M. Buchner, C. Rizzo, and J. Vigué. The three-grating Mach-Zehnder optical interferometer: A tutorial approach using particle optics. *Eur. J. Phys.*, 23(6):623–635, 2002.

[50] Ch J. Bordé, N. Courtier, F. du Burck, A. N. Goncharov, and M. Gorlicki. Molecular interferometry experiments. *Phys. Lett. A*, 188(3):187–197, 1994.

[51] Klaus Hornberger, Stefan Gerlich, Philipp Haslinger, Stefan Nimmrichter, and Markus Arndt. Colloquium: Quantum interference of clusters and molecules. *Rev. Mod. Phys.*, 84(1):157–173, 2012.

[52] H.F. Talbot. LXXVI. Facts relating to optical science. No. IV. *Philos. Mag. Ser. 3*, 9(56):401–407, 1836.

[53] Stefan Nimmrichter. *Macroscopic Matter-wave Interferometry.* Phd thesis, University Vienna, 2013.

[54] William B. Case, Mathias Tomandl, Sarayut Deachapunya, and Markus Arndt. Realization of optical carpets in the Talbot and Talbot-Lau configurations. *Opt. Express*, 17(23):20966, 2009.

[55] Emil Lau. Beugungserscheinungen an Doppelrastern. *Ann. Phys.*, 6:417, 1948.

[56] P. H. van Cittert. Die wahrscheinliche Schwingungsverteilung in einer von einer Lichtquelle direkt oder mittels einer Linse beleuchteten Ebene. *Physica*, 1:201–210, 1934.

[57] F. Zernike. The concept of degree of coherence and its application to optical problems. *Physica*, 5(8):785–795, 1938.

[58] Björn Brezger, Markus Arndt, and Anton Zeilinger. Concepts for near-field interferometers. *J. Opt. B Quantum Semiclassical Opt.*, 5:82–89, 2003.

[59] N. Schmailzer. The effects of Talbot and Lau. *Report*, 21(1):1–3, 2014.

[60] W. Heisenberg. Über den anschaulichen Inhalt der quantentheoretischen Kinematik und Mechanik. *Zeitschrift für Phys.*, 43(3-4):172–198, 1927.

[61] Thomas Juffmann, Stefan Truppe, Philipp Geyer, Andreas G. Major, Sarayut Deachapunya, Hendrik Ulbricht, and Markus Arndt. Wave and particle in molecular interference lithography. *Phys. Rev. Lett.*, 103(26):1–4, 2009.

[62] Björn Brezger, Lucia Hackermüller, Stefan Uttenthaler, Julia Petschinka, Markus Arndt, and Anton Zeilinger. Matter-Wave Interferometer for Large Molecules. *Phys. Rev. Lett.*, 88(10):100404, 2002.

[63] R. Brühl, P. Fouquet, R. E. Grisenti, J. P. Toennies, G. C. Hegerfeldt, T. Köhler, M. Stoll, and C. Walter. The van der Waals potential between metastable atoms and solid surfaces: Novel diffraction experiments vs. theory. *Europhys. Lett.*, 59(3):357–363, 2002.

[64] John D. Perreault and Alexander D. Cronin. Measurement of atomic diffraction phases induced by material gratings. *Phys. Rev. A - At. Mol. Opt. Phys.*, 73(3):1–5, 2006.

[65] Philipp Haslinger, Nadine Dörre, Philipp Geyer, Jonas Rodewald, Stefan Nimmrichter, and Markus Arndt. A universal matter-wave interferometer with optical ionization gratings in the time domain. *Nat. Phys.*, 9(3):144–148, 2013.

[66] S. B. Cahn, A. Kumarakrishnan, U. Shim, T. Sleator, P. R. Berman, and B. Dubetsky. Time-domain de broglie wave interferometry. *Phys. Rev. Lett.*, 79(5):784–787, 1997.

[67] L. Deng, E. W. Hagley, J. Denschlag, Simsarian J. E., M Edwards, C. W. Chlark, K. Helmerson, S. L. Rolston, and W. D. Phillips. Temporal, Matter-Wave-Dispersion Talbot Effect. *Phys. Rev. Lett.*, 83(26):1–5, 1999.

[68] Sebastian Fray, Cristina Alvarez Diez, Theodor W. Hänsch, and Martin Weitz. Atomic interferometer with amplitude gratings of light and its applications to atom based tests of the equivalence principle. *Phys. Rev. Lett.*, 93(24):1–4, 2004.

[69] Nadine Dörre, Jonas Rodewald, Philipp Geyer, Bernd Von Issendorff, Philipp Haslinger, and Markus Arndt. Photofragmentation beam splitters for matter-wave interferometry. *Phys. Rev. Lett.*, 113(23):1–5, 2014.

[70] Stefan Gerlich, Lucia Hackermüller, Klaus Hornberger, Alexander Stibor, Hendrik Ulbricht, Michael Gring, Fabienne Goldfarb, Tim Savas, Marcel Müri, Marcel Mayor, and Markus Arndt. A Kapitza-Dirac-Talbot-Lau interferometer for highly polarizable molecules. *Nat. Phys.*, 3(10):711–715, 2007.

[71] Shau Yu Lan, Pei Chen Kuan, Brian Estey, Philipp Haslinger, and Holger Müller. Influence of the coriolis force in atom interferometry. *Phys. Rev. Lett.*, 108(9):1–5, 2012.

[72] Klaus Hornberger, John E. Sipe, and Markus Arndt. Theory of decoherence in a matter wave Talbot-Lau interferometer. *Phys. Rev. A - At. Mol. Opt. Phys.*, 70(5 B), 2004.

[73] Stefan Nimmrichter and Klaus Hornberger. Theory of near-field matter-wave interference beyond the eikonal approximation. *Phys. Rev. A - At. Mol. Opt. Phys.*, 78(2):1–18, 2008.

[74] Stefan Nimmrichter, Philipp Haslinger, Klaus Hornberger, and Markus Arndt. Concept of an ionizing time-domain matter-wave interferometer. *New J. Phys.*, 13, 2011.

[75] Jonas Rodewald. *Experiments with a pulsed Talbot Lau matter-wave interferometer.* Phd thesis, University of Vienna, 2017.

[76] Nadine Dörre. *Time-domain matter-wave interferometry with clusters and large molecules.* Phd thesis, University of Vienna, 2015.

[77] Philipp Geyer. *Matter-wave interferometry with complex nanoparticles.* Phd thesis, University of Vienna, 2015.

[78] E. Wigner. On the quantum correction for thermodynamic equilibrium. *Phys. Rev.*, 40(5):749–759, 1932.

[79] Arndold Sommerfeld. *Optik, Vorlesungen über Theoretische Physik Vol. IV.* Dieterichsche Verlagsbuchhandlung, 1950.

[80] Stefan Nimmrichter. *Matter wave Talbot-Lau interferometry beyond the eikonal approximation.* Diploma thesis, Technische Universität München, 2007.

[81] Markus K. Oberthaler, Stefan Bernet, Ernst M. Rasel, Jörg Schmiedmayer, and Anton Zeilinger. Inertial sensing with classical atomic beams. *Phys. Rev. A - At. Mol. Opt. Phys.*, 54(4):3165–3176, 1996.

[82] J. Bremer, R. S. Brusa, L. Cabaret, C. Canali, R. Caravita, F. Castelli, G. Cerchiari, S. Cialdi, R. Ferragut, A. Fontana, P. Genova, M. Giammarchi, A. Gligorova, S. N. Gninenko, S. Haider, and T. Huse. A moire deflectometer for antimatter. *Nat. Commun.*, 5:1–6, 2014.

[83] Jonas Rodewald, Nadine Dörre, Andrea Grimaldi, Philipp Geyer, Lukas Felix, Marcel Mayor, Armin Shayeghi, and Markus Arndt. Isotope-selective high-order interferometry with large organic molecules in free fall. *New J. Phys.*, 20(033016), 2018.

[84] Klaus Hornberger, Stefan Uttenthaler, Björn Brezger, Lucia Hackermüller, Markus Arndt, and Anton Zeilinger. Collisional Decoherence Observed in Matter Wave Interferometry. *Phys. Rev. Lett.*, 90(16):4, 2003.

[85] T.A. Cross, F. Tian, M. Cotten, J. Wang, F. Kovacs, and R. Fu. Correlations of structure, dynamics and function in the gramicidin channel by solid-state NMR spectroscopy. *ChemInform*, 32(2), 2001.

[86] Zhangfei Su, Jay J. Leitch, Robert J. Faragher, Adrian L. Schwan, and Jacek Lipkowski. Gramicidin A ion channel formation in model phospholipid bilayers tethered to gold111 electrode surfaces. *Electrochim. Acta*, 243:364–373, 2017.

[87] U. Even. The Even-Lavie valve as a source for high intensity supersonic beam. *EPJ Tech. Instrum.*, 2(1):1–22, 2015.

[88] X. Liu, D. Du, and G. Mourou. Laser Ablation and Micromachining with Ultrashort Laser Pulses. *IEEE J. Quantum Electron.*, 33(10):1706–1716, 1997.

[89] Richard Knochenmuss. Ion formation mechanisms in UV-MALDI. *Analyst*, 131(9):966–986, 2006.

[90] Paul Flanigan and Robert Levis. Ambient Femtosecond Laser Vaporization and Nanosecond Laser Desorption Electrospray Ionization Mass Spectrometry. 2014.

[91] John J. Brady, Elizabeth J. Judge, and Robert J. Levis. Analysis of Amphiphilic Lipids and Hydrophobic Proteins Using Nonresonant Femtosecond Laser Vaporization with Electrospray Post-Ionization. *J. Am. Soc. Mass Spectrom.*, 22(4):762–772, 2011.

[92] Elizabeth J. Judge, John J. Brady, and Robert J. Levis. Mass Analysis of Biological Macromolecules at Atmospheric Pressure Using Nonresonant Femtosecond Laser Vaporization and Electrospray Ionization. *Anal. Chem.*, 82(24):10203–10207, 2010.

[93] Klaus Dreisewerd and Franz Hillenkamp. Influence of the laser intensity and spot size on the desorption of molecules and ions in matrix-assisted laser desorption / ionization with a uniform beam profile. 141:127–148, 1995.

[94] S. M. Hooker and C. E. Webb. Progress in vacuum ultraviolet lasers. *Prog. Quantum Electron.*, 18(3):227–274, 1994.

[95] C. J. Sansonetti, J. Reader, and K. Vogler. Precision measurement of wavelengths emitted by a molecular fluorine laser at 157 nm. *Appl. Opt.*, 40(12):1974–8, 2001.

[96] K. Yoshino, W. H. Parkinson, K. Ito, and T. Matsui. Absolute absorption cross-section measurements of Schumann-Runge continuum of O2at 90 and 295 K. *J. Mol. Spectrosc.*, 229(2):238–243, 2005.

[97] C. Görling, U. Leinhos, and K. Mann. Surface and bulk absorption in CaF2at 193 and 157 nm. *Opt. Commun.*, 249(1-3):319–328, 2005.

[98] A. K. Bates, M. Rothschild, T. M. Bloomstein, T. H. Fedynyshyn, R. R. Kunz, V. Liberman, and M. Switkes. Review of technology for 157-nm lithography. *IBM J. Res. Dev.*, 45(5):605–614, 2001.

[99] Nadine Dörre, Philipp Haslinger, Jonas Rodewald, Philipp Geyer, and Markus Arndt. Refined model for Talbot–Lau matter-wave optics with pulsed photodepletion gratings. *J. Opt. Soc. Am. B*, 32(1):114, 2015.

[100] W. C. Wiley and I. H. McLaren. Time-of-flight mass spectrometer with improved resolution. *Rev. Sci. Instrum.*, 26(12):1150–1157, 1955.

[101] Markus Arndt, Nadine Dörre, Sandra Eibenberger, Philipp Haslinger, Jonas Rodewald, Klaus Hornberger, Stefan Nimmrichter, and Marcel Mayor. Matter-wave interferometry with composite quantum objects. *Atom Interferom. Proc. Int. Sch. Phys. "Enrico Fermi"*, 188, 2015.

[102] Lynn J. Rothschild and Rocco L. Mancinelli. Life in extreme environments. *Nature*, 409(6823):1092–1101, 2001.

[103] Arthur Ashkin and J. Dziedzic. Optical trapping and manipulation of viruses and bacteria. *Science (80-.).*, 235(4795):1517–1520, 1987.

[104] G. Habermehl, P. Hammann, H. Krebs, and W. Ternes. *Naturstoffchemie - Eine Einfuehrung*. 3 edition, 2008.

[105] Benjamin Lasorne, Graham A. Worth, and Michael A. Robb. Excited-state dynamics. *WIREs Comput Mol Sci*, 1:260–475, 2011.